

Development of stiffness sensing and adaptive grasping with soft pneumatic grippers



A Dissertation Submitted in Partial Fulfillment of the Requirements
for the Degree of Doctor of Philosophy in Mechanical Engineering

Department of Mechanical Engineering

FACULTY OF ENGINEERING

Chulalongkorn University

Academic Year 2022

Copyright of Chulalongkorn University

การพัฒนาวิธีการรับรู้ความแข็งของวัสดุและการจับแบบปรับได้ด้วยมือจับนิวมเมติกแบบอ่อน



วิทยานิพนธ์นี้เป็นส่วนหนึ่งของการศึกษาตามหลักสูตรปริญญาวิศวกรรมศาสตรดุษฎีบัณฑิต
สาขาวิชาวิศวกรรมเครื่องกล ภาควิชาวิศวกรรมเครื่องกล
คณะวิศวกรรมศาสตร์ จุฬาลงกรณ์มหาวิทยาลัย
ปีการศึกษา 2565
ลิขสิทธิ์ของจุฬาลงกรณ์มหาวิทยาลัย

Thesis Title Development of stiffness sensing and adaptive grasping
with soft pneumatic grippers
By Mr. Chaiwuth Sithiwichankit
Field of Study Mechanical Engineering
Thesis Advisor Associate Professor RATCHATIN CHANCHAROEN, Ph.D.

Accepted by the FACULTY OF ENGINEERING, Chulalongkorn University in
Partial Fulfillment of the Requirement for the Doctor of Philosophy

----- Dean of the FACULTY OF
ENGINEERING
(Professor SUPOT TEACHAVORASINSKUN, D.Eng.)

DISSERTATION COMMITTEE

----- Chairman
(Associate Professor Jiraphon Srisertpol, Ph.D.)
----- Thesis Advisor
(Associate Professor RATCHATIN CHANCHAROEN, Ph.D.)
----- Examiner
(Professor PAIROD SINGHATANADGID, Ph.D.)
----- Examiner
(Associate Professor ALONGKORN PIMPIN, D.Eng.)
----- Examiner
(Associate Professor GRIDSADA PHANOMCHOENG, Ph.D.)

ชัชวาลย์ สิทธิวิจารณ์กิจ : การพัฒนาวิธีการรับรู้ความแข็งของวัตถุและการจับแบบปรับได้
ด้วยมือจับนิวแมติกแบบอ่อน. (Development of stiffness sensing and adaptive
grasping with soft pneumatic grippers) อ.ที่ปรึกษาหลัก : รศ. ดร.รัชทิน จันทร
เจริญ

การศึกษานี้ครอบคลุมการพัฒนาเพื่อรับรู้ความแข็งของวัตถุโดยการจับด้วยมือจับนิวแมติกแบบอ่อน และปรับการจับให้เหมาะสมตามความแข็งของวัตถุที่วัดได้ โดยได้รับแรงบันดาลใจจากความสามารถในการรับรู้ความแข็งของวัตถุผ่านการจับและการจับวัตถุที่ซับซ้อนของมนุษย์ สาเหตุของความยากและซับซ้อนคือความยืดหยุ่นของมือจับนิวแมติกแบบอ่อน การศึกษานี้นำเสนอความเชื่อมโยงระหว่างพฤติกรรมของวัตถุที่ถูกจับและการทำงานของมือจับ แนวทางใหม่ในการสร้างแบบจำลองของมือจับ และระเบียบวิธีในการวัดความแข็งของวัตถุผ่านการทำงานของมือจับ จากนั้นนำผลลัพธ์จากระเบียบวิธีดังกล่าวไปเปรียบเทียบกับผลที่ได้จากการทดสอบการบีบอัด โดยผลลัพธ์ทั้งสองชุดมีลักษณะคล้ายกันและมีความคลาดเคลื่อนเล็กน้อย นอกจากนี้การศึกษายังนำเสนอวิธีการจำลองการยุบตัวและแรงบนวัตถุขณะถูกจับด้วยมือจับ และวิธีการควบคุมการทำงานของมือจับที่ปรับตามความแข็งของวัตถุ วิธีการดังกล่าวให้ผลลัพธ์เชิงการยุบตัวที่คาดเคลื่อนในกรอบที่ยอมรับได้ ขณะที่ผลลัพธ์เชิงแรงมีความคลาดเคลื่อนสูง ข้อจำกัดสำคัญในการศึกษานี้คือการวัดระยะกดของมือจับด้วยภาพถ่าย ซึ่งมีข้อจำกัดด้านความแม่นยำ โดยภาพรวมการศึกษานี้เป็นงานแรกที่บูรณาการการวัดความแข็งของวัตถุเข้ากับการจับวัตถุด้วยมือจับนิวแมติกแบบอ่อน และนำเสนอวิธีการที่สามารถควบคุมพฤติกรรมของวัตถุขณะที่ถูกจับด้วยมือจับนิวแมติกแบบอ่อนได้ โดยภาพรวมการศึกษานี้นำไปสู่การพัฒนาในสาขาวิทยาการหุ่นยนต์แบบอ่อนและการจำแนกวัตถุ

สาขาวิชา วิศวกรรมเครื่องกล

ลายมือชื่อนิสิต

ปีการศึกษา 2565

ลายมือชื่อ อ.ที่ปรึกษาหลัก

6371006021 : MAJOR MECHANICAL ENGINEERING

KEYWORD: soft gripper, pneumatic gripper, pincer grasping, adaptive grasping,
sensible grasping, stiffness sensing

Chaiwuth Sithiwichankit : Development of stiffness sensing and adaptive grasping with soft pneumatic grippers. Advisor: Assoc. Prof. RATCHATIN CHANCHAROEN, Ph.D.

This study presents a framework for stiffness sensing and adaptive grasping using soft pneumatic grippers (SPGs). The motivation was to imitate the capabilities of human hands. The challenge was the compliance of soft pneumatic actuators (SPAs). The study associated the behaviors of grasped objects with those on SPAs, introduced a new concept of SPA modeling, and proposed a method for stiffness sensing through SPG pincer grasping. Compression testing was conducted for validation. A technique for forecasting deformation and force on grasped objects based on their stiffness was established, and a control law was elaborated. The presented technique and control architecture were validated at different input pressure conditions. The proposed method yielded similar stiffness trends with slight deviations compared to compression testing and demonstrated the potential for manual classification of samples. The presented technique provided small deviations in deformation but significant errors in force. A major limitation was caused by the using of computer vision for inspecting SPA deformation. To overcome this limitation further studies on the direct sensing of SPA deformation is recommended. Overall, this study contributes to the field of soft robotics and object classification by integrating stiffness sensing and SPG grasping in a single action, leading to the next level of adaptive SPG grasping.

Field of Study: Mechanical Engineering

Student's Signature

Academic Year: 2022

Advisor's Signature

ACKNOWLEDGEMENTS

I would like to express my gratitude and appreciation to my advisor, Assoc. Prof. Ratchatin Chanchareon, Ph.D., for his unwavering support, guidance, and expertise throughout my doctoral journey. His mentorship and insightful feedback have been invaluable in shaping the direction and quality of this research.

I am also grateful to the members of my dissertation committee, Professor Pairod Singhatanadgid, Ph.D., Assoc. Prof. Alongkorn Pimpin, D.Eng, Assoc. Prof. Gridsada Phanomchoeng, Ph.D., and Assoc. Prof. Jiraphon Srisertpol, Ph.D., for their time, expertise, and valuable input during the development and evaluation of this work. Their constructive comments and suggestions have significantly enhanced the rigor and relevance of this study.

I extend my sincere appreciation to Chulalongkorn University for providing the necessary resources, facilities, and funding that made this research possible. The collaborative environment and access to cutting-edge technologies have been instrumental in conducting experiments and analyzing data effectively. In addition, I would like to address that I am supported by a scholarship from “The 100th Anniversary Chulalongkorn University Fund for Doctoral Scholarship.”

Lastly, I would like to express my heartfelt appreciation to my parents, Mr. Suchat and Mrs. Aree Sithiwichankit, for their unwavering love, encouragement, and belief in my abilities. Their unwavering support and understanding have been a constant source of motivation and inspiration throughout this challenging endeavor.

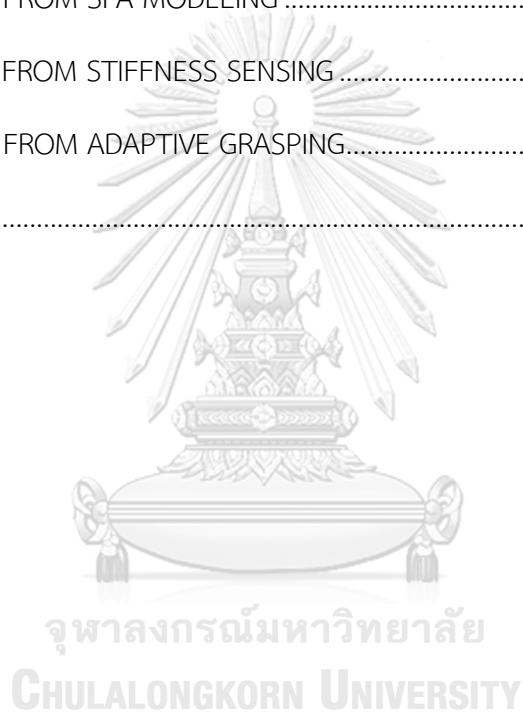
This research would not have been possible without the support and contributions of all those mentioned above. While any shortcomings in this work are solely my responsibility, their collective efforts have undoubtedly played a significant role in its success.

Chaiwuth Sithiwichankit

TABLE OF CONTENTS

	Page
ABSTRACT (THAI)	iii
ABSTRACT (ENGLISH)	iv
ACKNOWLEDGEMENTS	v
TABLE OF CONTENTS	vi
CHAPTER I: INTRODUCTION.....	1
1.1 Background	1
1.2 Challenges.....	3
1.3 Scope and Contributions.....	3
CHAPTER II: LITERATURE REVIEW	5
2.1 Robotic Gripper	5
2.2 Robotic Modeling	7
2.3 SPA Modeling.....	9
2.4 Stereo Computer Vision.....	12
CHAPTER III: METHODOLOGY.....	15
3.1 Stiffness Measurement.....	15
3.2 SPG Pincer Grasping	15
3.3 SPA Modeling.....	17
3.4 Stiffness Sensing Through SPG Pincer Grasping.....	21
3.5 Validation of Stiffness Sensing Through SPG Pincer Grasping.....	25
3.6 Adaptive SPG Pincer Grasping Based on Object Stiffness.....	26
CHAPTER IV: RESULTS AND DISSCUSSION.....	29

4.1 SPA Modeling.....	29
4.2 Stiffness Sensing Through SPG Pincer Grasping.....	29
4.3 Validation of Stiffness Sensing Through SPG Pincer Grasping.....	33
4.4 Adaptive SPG Pincer Grasping Based on Object Stiffness.....	36
CHAPTER V: CONCLUSION.....	40
REFERENCES.....	42
APPENDIX A: DATA FROM SPA MODELING	51
APPENDIX B: DATA FROM STIFFNESS SENSING	53
APPENDIX C: DATA FROM ADAPTIVE GRASPING.....	67
VITA.....	73



CHAPTER I: INTRODUCTION

1.1 Background

A robotic system is basically one or a group of machine that capable of performing complex operations following a computer program.^{1,2} Its operation can be flexibly designed for various applications, such as manufacturing, inspection, exploration, and transportation.³ Nowadays, robotic systems are increasingly important in modern society as they can complete tasks that difficult or impossible for humans.⁴ One of their most essential components is gripper.⁵⁻⁸ Robotic grippers are commonly equipped to robotic manipulators and mainly responsible for grasping objects.⁹⁻¹¹ The grippers come in various shapes, sizes, and working principles.¹² Based on the working principle, the grippers can be categorized into four main groups, including impactive, ingressive, astrictive, and contigutive.¹³

Developers of robotic grippers have been studied on human hand for inspiration in creating grippers with similar functionality and capabilities.¹⁴⁻¹⁷ One of the most interesting features of human hand is haptic sensing, which allows us to perceive the mechanical properties of objects we grasp and adjust the motion and force of our fingers accordingly throughout grasping.¹⁸ The developers have been inspired by this feature and are working to bring it into robotic systems. The systems with this feature have the potential to be more effective in the terms of working cost, space, and time for object classification and identification across a wide spectrum of applications.^{19, 20} This capability can also facilitate adaptive grasping based on the mechanical properties of grasped objects, and enable further advancements in the field.

Researchers have conducted numerous studies on the sensing of mechanical properties through impactive grippers. However, most of such studies have focused on conventional impactive grippers, commonly known as mechanical grippers.²¹⁻²⁴ The researchers integrated various types of sensors onto the grippers to measure their internal states, external inputs, and loads. The sensors utilized in these studies were primarily visual, force, and tactile types.^{25, 26} In cases that such variables could not be directly measured, kinematic and kinetic models of the grippers were developed and

employed to determine them. The connection between variables on the grippers and those on grasped objects was solved. Afterwards, the properties of the objects were observed through the variables on the grippers. For example, Kim²⁷ integrated a force sensor to a mechanical gripper in estimating object weight. Romano et al.²⁸ developed a human-inspired adaptive grasping technique using a mechanical gripper with tactile sensors. Spiers et al.^{29, 30} investigated feature extraction, shape recognition, and object classification using various types of mechanical grippers.

During several recent decades, soft gripper has been growing attention as a new and interesting class of grippers.³¹⁻³³ Soft grippers were designed to be structurally compliant, and some of them are impactive type. A key feature of the soft grippers is their mechanical intelligence, which allows them to grasp dissimilar objects using simple control architectures.³⁴⁻³⁶ A popular type of soft grippers is soft pneumatic gripper (SPG), the working principle of which relies on anisotropic inflation based on pressurized air. SPGs typically consist of two or more soft pneumatic actuators (SPAs) that have flexible structures.³⁷⁻³⁹ Only a few of studies have explored the potential of SPG grasping in the context of sensing. For instance, Homberg et al.⁴⁰ used data-driven haptic identification to recognize objects using SPGs. Chen et al.⁴¹ demonstrated adaptive grasping and size recognition with SPGs. Sankar et al.⁴² investigated the discrimination of textures using SPGs. These studies primarily focused on the geometrical features and surface properties of objects, rather than their mechanical characteristics.

Adaptive grasping is a field of robotics, which involves designing and developing robotic systems capable of grasping objects in unstructured environments.^{43, 44} The primary objective of this field is to equip robotic systems with the ability to handle objects with diverse characteristics, including shape, size, and texture, without any prior knowledge of the objects.^{29, 45} This capability is critical in many applications where robotic systems are utilized to manipulate a vast array of objects. To achieve adaptive grasping, diverse techniques are employed to enable robotic systems to perceive object properties and adjust their grasping strategy based on the properties of the objects.⁴⁶ If object properties can be observed through grasping, adaptive grasping of

robotic systems is expected to be revolutionized made more efficient, like that performed by humans.

1.2 Challenges

SPAs are typically made of various elastomers, which offer admirable flexibility and compliance.^{47, 48} SPA compliance makes the modeling of SPAs and SPG grasping complicated, because SPA structures have infinite degree of freedom (DOF) with nonlinear characteristics. Conventional modeling methods rely on local-joint variables, and only suitable for systems with finite DOF.⁴⁹ Such methods thus cannot be used to model SPAs or SPG grasping. Some researchers have proposed simulation approaches to overcome this challenge, however available simulation solvers are not designed to handle the enormous magnitude of deformation occurring on SPA bodies.^{50, 51} Compared to the modeling of SPAs, there is much less information available on the modeling of SPG grasping. Consequently, the modeling of SPAs and SPG grasping remains a sophisticated problem.

1.3 Scope and Contributions

This dissertation aims to develop a novel approach for sensing object stiffness through SPG pincer grasping, and adaptively grasping objects based on their stiffness. To achieve this goal, SPG pincer grasping was first observed, and then the association between the deformation and force on SPAs and those on grasped objects was investigated and formulated. A new concept of SPA modeling was also elaborated and implemented on an industrial SPA. Afterwards, an innovative method of stiffness sensing through SPG pincer grasping was developed. The developed method was applied to four elastic samples using an SPG, the SPAs of which are identical to the one examined with the presented SPA-modeling concept. Later, compression testing was conducted on the same samples. The results of stiffness obtained from both methods were compared to validate the proposed method. Later, a technique for modeling the deformation and force on grasped objects, with respect to the input pressure of SPAs, throughout SPG pincer grasping was established, together with an opened-loop control architecture for accomplishing desirable deformation and force

on the objects. The presented techniques of modeling and control was practiced on the samples, and the deformation and force on the samples were then practically measured for validation. The contribution and novelty of this study are that it is the first study to combine stiffness sensing and SPG grasping in a single action, and utilize the resulting stiffness to perform adaptive SPG grasping based on object stiffness. Therefore, this study makes a considerable advancement in the field of soft robotics, for connecting SPG grasping to a new sensing application, and progressing leading to a novel form of adaptive SPG grasping. In addition, the study contributes to the area of object classification, by offering another class of classification data with an efficient approach of data acquisition.



CHAPTER II: LITERATURE REVIEW

2.1 Robotic Gripper

Grippers are necessary in robotics and other forms of automation, for grasping objects. They are typically equipped to the moving ends of robotic manipulators, and enable robotic systems to have physical interaction with objects.⁵⁻⁸ This interaction can be exploited for mechanical object manipulation.⁹⁻¹¹ There are many types of robotic grippers that can be classified according to various criteria (Figure 1), such as finger number, actuation type, mechanism type, grasping mode, and grasping principle.¹² Grippers of different types are suitable for grasping objects with different properties. The most comprehensive classification strategy is based on the principle of grasping, which categorizes robotic grippers into four main groups: impactive, ingressive, astrictive, and contigutive.¹³ The majority of industrial grippers are either impactive or astrictive. The following list provides details on each type of gripper.

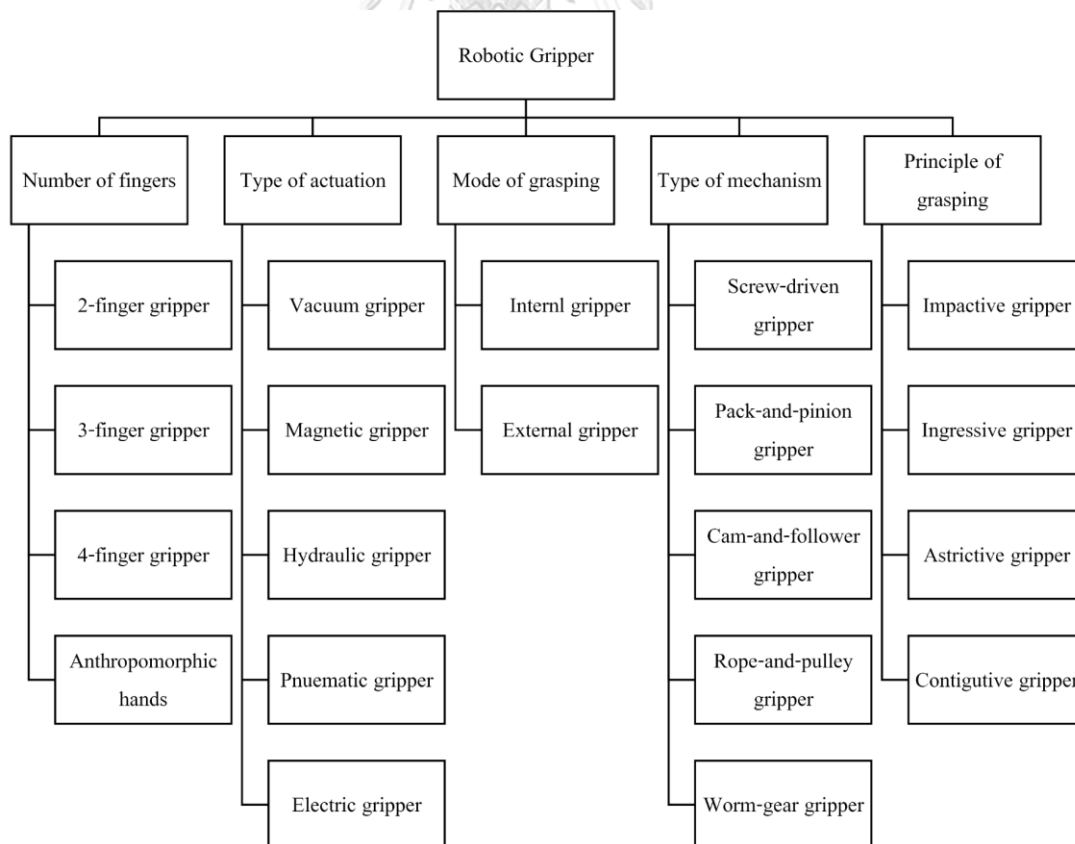


FIGURE 1. Gripper classification based on different strategies of classification.¹²



FIGURE 2. Robotic grippers: **(a)** mechanical gripper⁵²; **(b)** pin-array gripper⁵³; **(c)** vacuum gripper⁵⁴; and **(d)** adhesive gripper⁵⁵.

- Impactive gripper is the type of gripper that conduct impactive force against the surface of objects. Grippers of this type have two or more fingers to produce impactive force, and operate like human hand. The vastest instance of impactive gripper is mechanical gripper (Figure 2a).
- Ingressive gripper is the type of gripper that permeate objects. The permeation can be either intrusive or non-intrusive. Pin-array gripper (Figure 2b) is an example of intrusive gripper, while hook-and-loop gripper is an instance of non-intrusive gripper.

- Atractive is the type of gripper that generate some kinds of field, such as air flow, magnetic, and electric, to make binding force. Vacuum gripper (Figure 2c) is the most widespread example of the grippers of this type.
- Contigutive is the type of gripper that directly make contact adhesion with object surface. The adhesion can be originated with various mechanisms, such as chemical reactions and thermal effects. An instance of contigutive gripper is adhesive gripper (Figure 2d).

2.2 Robotic Modeling

In conventional robotics, every system commonly consists of two fundamental components, links and joints.^{56, 57} These components are coupled into chain-like structures, allowing robots to have specific ranges of motion. Each link represents a rigid body with a certain shape and size. Designs of links can vary in design for particular requirements. Meanwhile, joints are mechanical components that connect two links and constrain relative motion between them. There are various types of joints widely used in robotics, such as revolute, prismatic, spherical, and planar. Different types of joints offers dissimilar forms of the relative motion between two links. The characteristics of robots depend on the combination of links and joints. Kinematic⁵⁸⁻⁶⁰ and dynamic⁶¹⁻⁶³ modeling are two essential approaches of modeling, for describing the behaviours of robotic systems.

Kinematics deals with the aspects of motion without any consideration in force. Kinematic modeling is accordingly the process of mathematically describing the positions, orientations, and motion of robot links. To handle the geometrical complexity of robots, a coordinate frame is widely attached to each robot link. Then, the association between a pair of robot links is described through the relationship between the corresponding frames. Denavit–Hartenberg parametes⁶⁴, including link length (a), link offset (d), link twist (α), and joint angle (θ), are the most widespread parameters for representing the kinematics of a robot. Such parameters indicate the relation of the current frame of consideration to the further frame (Figure 3). The

relationship between the $(i - 1)^{\text{th}}$ frame and i^{th} frame can be mathematically established with a homogeneous transformation as follows:

$${}^{i-1}H_i = \begin{bmatrix} \cos \theta_i & -\sin \theta_i \cos \alpha_i & \sin \theta_i \sin \alpha_i & a_i \cos \theta_i \\ \sin \theta_i & \cos \theta_i \cos \alpha_i & -\cos \theta_i \sin \alpha_i & a_i \sin \theta_i \\ 0 & \sin \alpha_i & \cos \alpha_i & d_i \\ 0 & 0 & 0 & 1 \end{bmatrix}. \quad (1)$$

Equation (1) is a straightforward solution for forward kinematics, as it explicitly offers the direct calculation of the positions and orientations of robot end-effectors, based on specific values of joint variables (d and θ). In contrast, solving inverse kinematics, in which the determination of the joint variables from the positions and orientation of the end-effectors is concerned, is much more challenging, because there is no systematic approach for this problem.

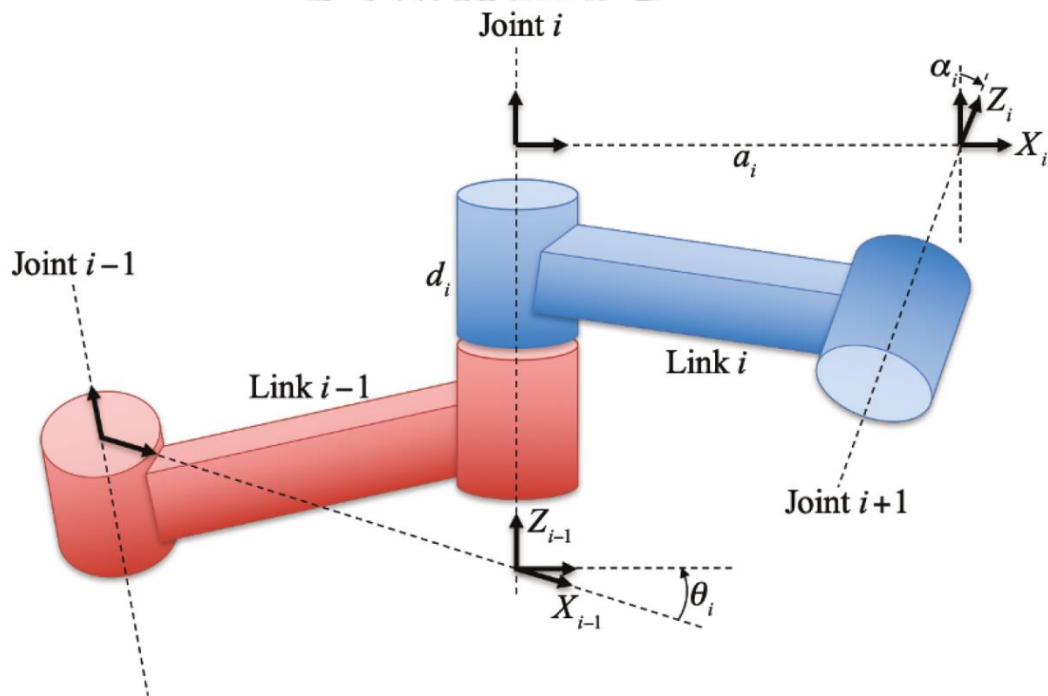


FIGURE 3. Denavit-Hartenberg parameters.⁶⁵

Dynamic modeling is basically the process of describing the motion of robots according to their forces and torques of internal and external. With a dynamic model, robot behaviours can be predictively determined. It is also extremely essential for robot control. Euler-Lagrange dynamic equation⁶⁶ is one of the most well-known

formulations for elucidating robot dynamics. The dynamics of a robot link can be generically written as follows:

$$\frac{d}{dt} \left(\frac{\partial L}{\partial \dot{q}_i} \right) + \frac{\partial L}{\partial q_i} = \tau_i, \quad (2)$$

where L is known as Lagrangian. Let T and V respectively denote the total kinetic and potential energy of the whole system of a robot, L was defined as $L = T - V$. Note that q_i and τ_i respectively represent the generic joint variable and force of the i^{th} link, while \dot{q}_i is the first-order derivative with respect to time of q_i . This equation is applicable for a broad range of robot types.

Equation (1) and (2) obviously illustrate that both kinematic and dynamic modeling in classical robotics rely on joint variables. Such approaches is technically viable only for robotic systems with countable numbers of joints. The modeling in the field of soft robotics, where robots are admirably compliance with infinite DOF, must be consequently succeeded following a new concept of modeling.

2.3 SPA Modeling

The modeling and control of SPAs has been a part of the mainstream research in soft robotics.⁶⁷⁻⁶⁹ The main cause of complication in this topic is that the admirable compliance of SPA structures comes with infinite DOF.^{47, 48} Most of SPAs are fabricated with some kinds of elastomer or fabric. These materials are continuously flexible and elastic, thus SPA structures commonly have infinite DOF with nonlinear characteristics. This issue makes conventional modeling methods, which rely on local-joint variables, unfunctional for SPA modeling, because the numbers of SPA local joints cannot be defined. The most usual technique to deal with the modeling of infinite-DOF systems is exploiting some combination effects of local joints to represent system configuration. Ordinarily, the assumption of constant curvature is applied in SPA modeling, and the configurations of SPAs are represented by SPA curvature (Figure 4).⁷⁰⁻⁷² Most of published works on SPA modeling were proceeded based on this concept, using either analytical or empirical approach. Some researchers also tried to elaborate curvature-based SPA models using simulation methods. Early models describe the correlation between the curvature and input air pressure of SPAs. In recent studies, the external

load at the free ends of SPAs is included in SPA models. Nevertheless, SPAs practically curve with increasing angle along SPA length during SPG pincer grasping (Figure 5). A novel idea of SPA modeling is hence needed for describing SPA performance throughout SPG pincer grasping. There is an adaptable concept of configurational representation in the work of Haibin et al.⁷³, where pincer grasping of soft cable-driven grippers was studied. The researchers recognized the configurations of gripper fingers through their transverse deformation (Figure 6).

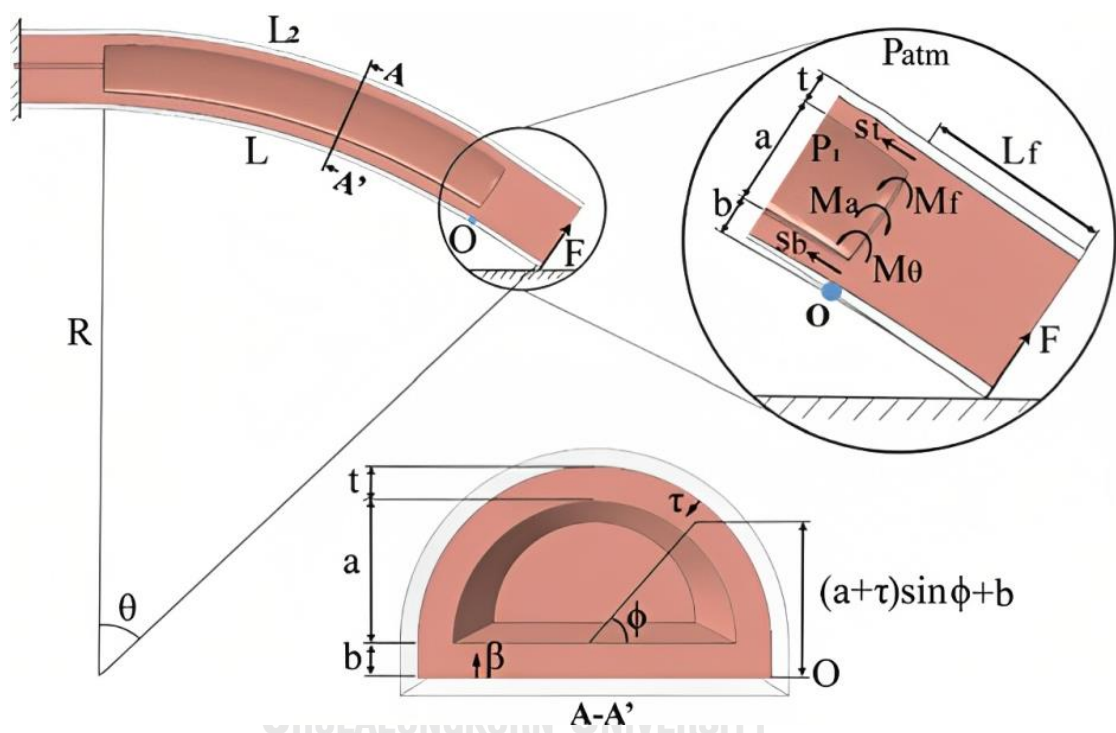


FIGURE 4. SPA modeling based on the assumption of constant curvature.⁷²



FIGURE 5. SPAs with continuously increasing angle of curvature along their length during SPG pincer grasping.

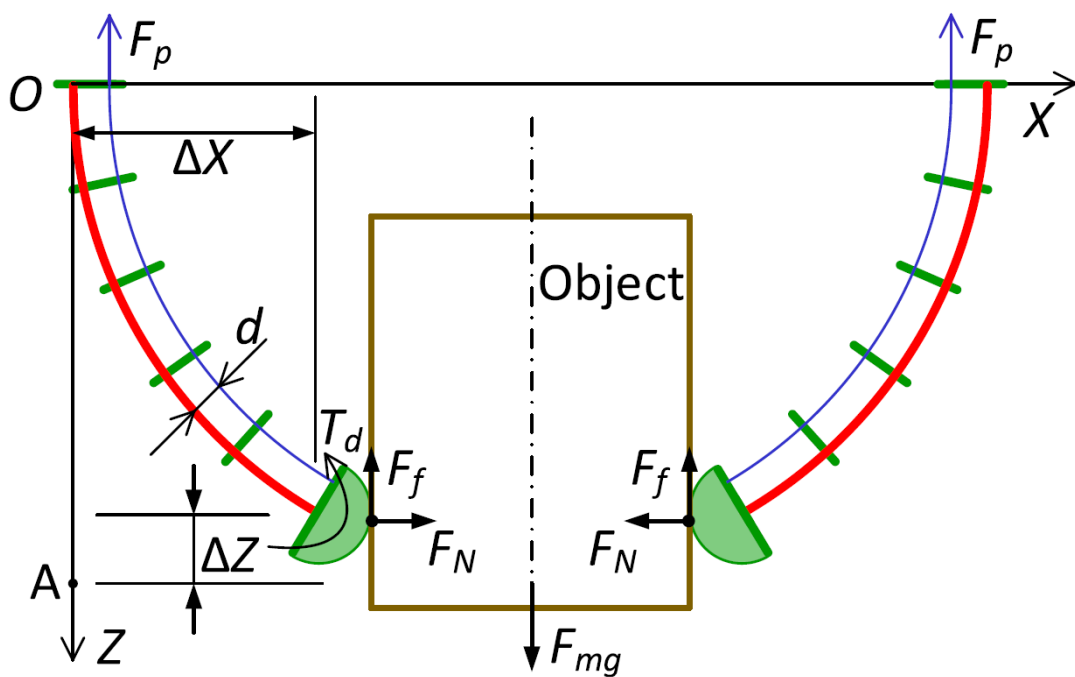


FIGURE 6. Pincer grasping of a soft cable-driven gripper with eight annotations of spatial and force.⁷³

2.4 Stereo Computer Vision

Computer vision is a field of study in computer science that focuses on making computers capable of understanding, interpreting, and analyzing visual information from digital images or videos.⁷⁴ Basically, it aims to imitate human vision capabilities to computers.⁷⁵ The development of in this field enables computers to perform various categories of tasks, such as object detection, facial recognition, and pose estimation. Accordingly, computer vision has been practically utilized in a wide range of other study fields, such as automotive⁷⁶, robotics⁷⁷, surveillance and security⁷⁸, medical⁷⁹, and agricultural⁸⁰. Stereo computer vision is the specific term referred to computer vision with multiple digital cameras.⁸¹ These cameras are typically positioned to capture different views of a scene. The disparity of images with different views of a scene allows three-dimensional (3D) spatial information to be extracted from the scene.⁸²

Pose estimation is the utilization of computer vision in determining the positions and orientations of designated features from one or a set of digital images.⁸³ It basically relies on image projection, the fundamental phenomenon during the acquisition of digital images, where light is projected onto sensing elements of digital cameras.⁸¹ One of the most extensive models for describing this phenomenon is central projection (Figure 7).⁸⁴ In this model, the rays of light direct from sources through the image plane to the center of projection, and the position and orientation of the image plane are relatively fixed to the center of projection. The intersection points of the rays on the image plane is literally the representation of the light sources on an image. Through the projection process, the 3D spatial information of a physical scene is reduced into two-dimensional (2D) information, represented in the images of the scene.⁸⁵ To overcome the information loss caused by image projection, the concept of stereo images, multiple images with different views of an identical scene, is widely employed (Figure 8).⁸⁶

Pose estimation with stereo images must be started with the calibration of the relative position and orientation of stereo cameras. Then, the corresponding points of features in the stereo images are identified. The disparity among the identified corresponding points is subsequently calculated. At this state, the distance in the

direction of dept can be estimated based on the calculated result of disparity. Finally, the 3D positions of the features with respect to the camera coordinate systems can be approximately reconstructed.

There is currently no complete solution for SPA sensing. Numerous developers exploited commercial resistive flex sensors to measure SPA curvature. Meanwhile, many researchers are working on elaborating novel intrinsically-soft sensors to perceive various proprioceptive parameters of SPAs. Pose estimation with stereo photographs of SPAs is a vastly-used method for recognizing SPA configuration. Several features on SPAs are frequently marked as the features for pose estimation.

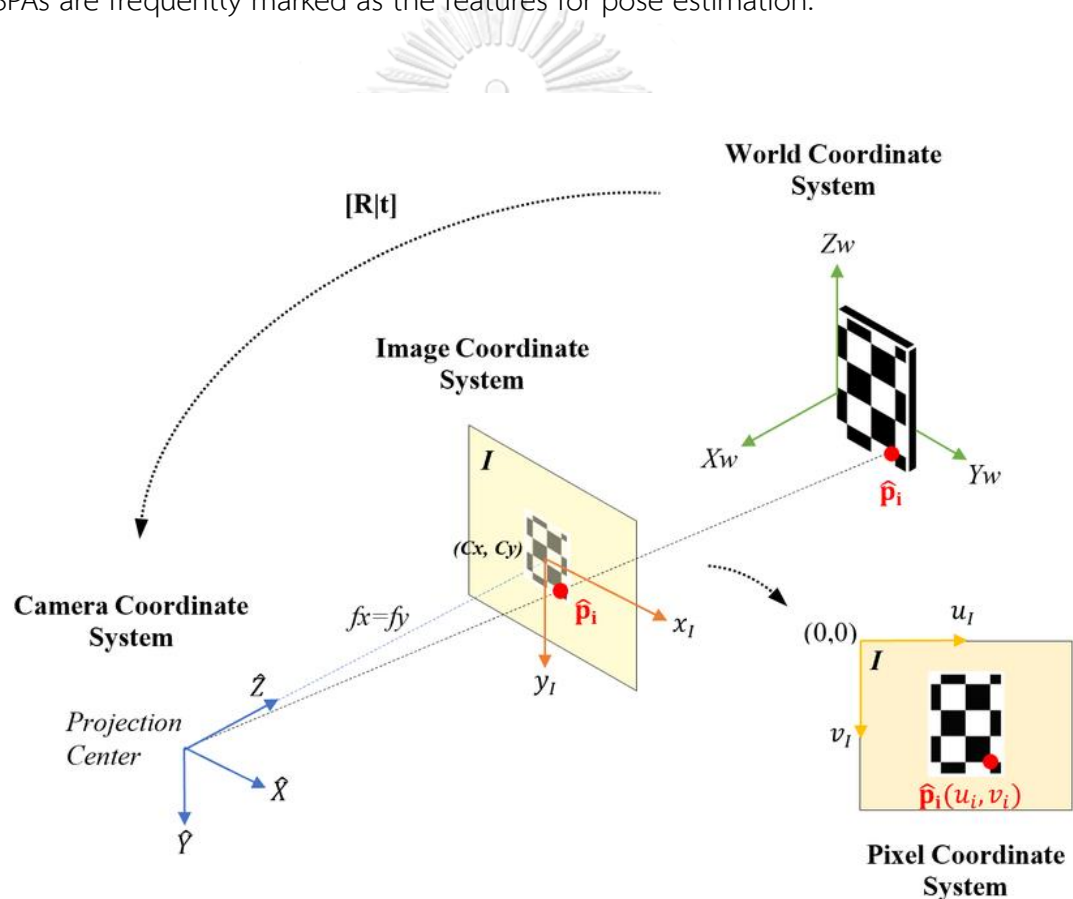


FIGURE 7. Central image projection of an ideal point onto a single image.⁸⁵

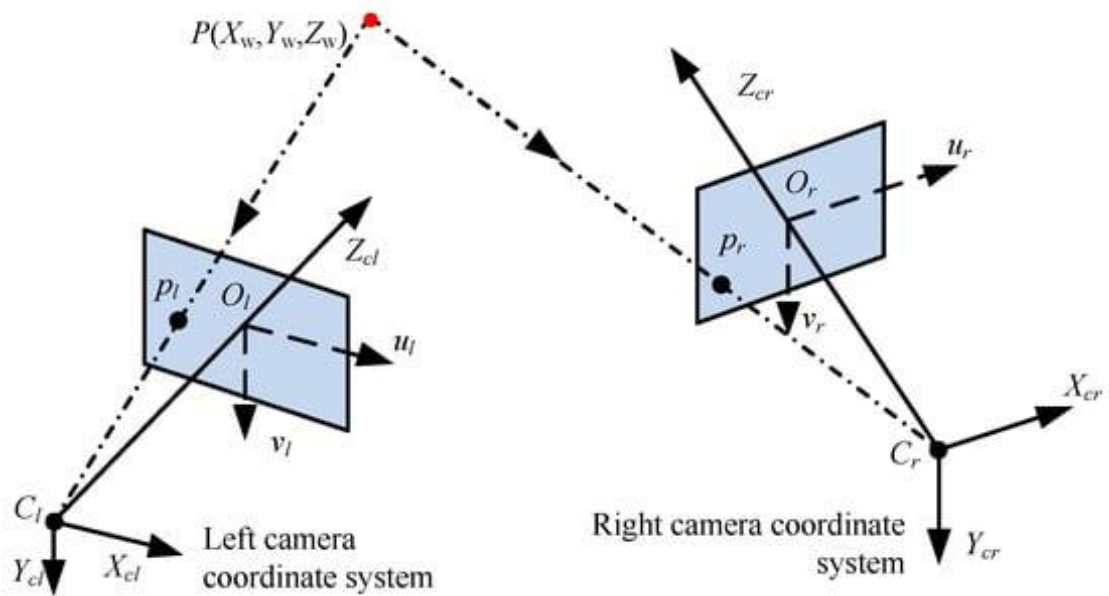


FIGURE 8. Central image projection of an ideal point onto a pair of stereo images.⁸⁶



CHAPTER III: METHODOLOGY

3.1 Stiffness Measurement

When an external force is applied to an object in the direction normal to object surface, the object deforms in the same direction (Figure 9). Stiffness is a mechanical property of an object that indicates its ability to withstand deformation under external-force loading. The magnitude of the deformation and force of the object are denoted by δ_0 and F_0 (Figure 9) respectively. The stiffness of the object, denoted by k_0 , relates δ_0 and F_0 as follows:

$$\partial F_0 = k_0(\delta_0) \cdot \partial \delta_0. \quad (3)$$

Rigid objects typically have consistent k_0 , while flexible objects have variable k_0 over δ_0 . Tensile⁸⁷ or compression⁸⁸ testing is a common method for investigating k_0 . These tests involve applying tension or compression loads to objects with specific machines, Meanwhile, the resulting series of δ_0 and F_0 are collected. Equation (1) is then employed to determine k_0 from the collected series of δ_0 and F_0 . During pincer grasping, grasped objects are also compressed by the fingertips of grippers. The interaction between the objects and grippers leads to the occurrence of δ_0 and F_0 . A series of δ_0 and F_0 recorded throughout pincer grasping is viable for determining k_0 following Equation (3). Therefore, there is the probability of sensing compressive k_0 through grasping.

3.2 SPG Pincer Grasping

Impactive grasping can be roughly classified into two main types: pincer and envelope grasping. In pincer grasping, objects are squeezed and held between the fingertips of grippers. Envelope grasping, on the other hand, involves using gripper fingers to confine objects, and the contact locations are unpredictable. In this study, we focused on pincer grasping of SPGs (Figure 9). The locations of the contact between SPAs and grasped objects can be assumed at SPA tips. The understanding in the interaction between each SPA and a grasped object is critical for associating the δ_0 and F_0 to the deformation and force of the SPA, denoted by δ_S and F_S (Figure 9).

Several factors, such as SPA performance, manipulator motion, and object weight, affect this interaction. To accurately perceive k_o through grasping, grasping conditions must be set up to minimize the effects of other factors besides SPA performance. Specifically, manipulators should be static, and additional support should be provided to compensate for the object weight.

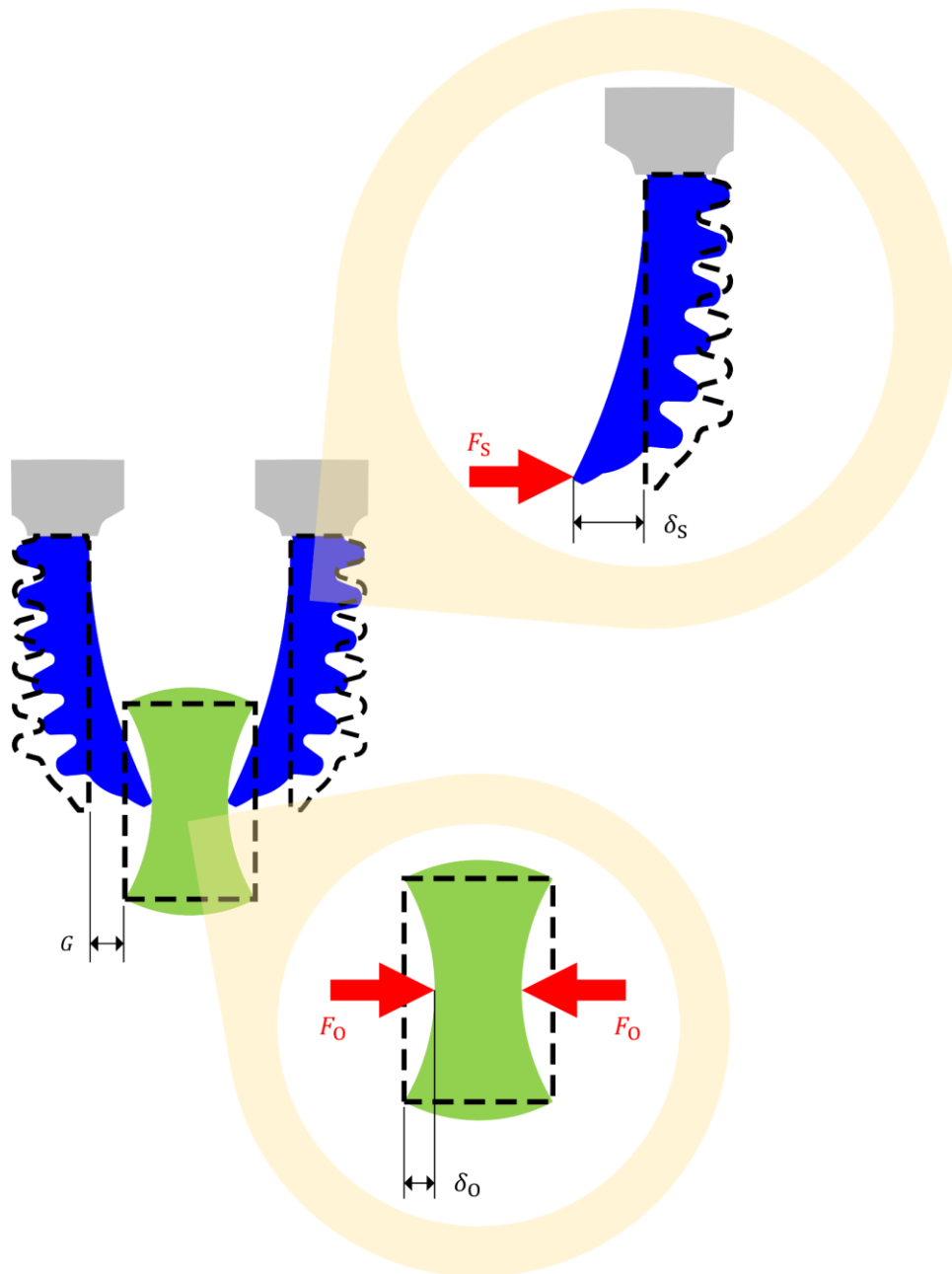


FIGURE 9. SPG pincer grasping on an object with deformation and force annotations on the SPA and object.

We observed and analyzed the pincer grasping of two-finger SPGs, and found that F_O algebraically correlates to F_S in magnitude as follows:

$$F_S(t) = F_O(t). \quad (4)$$

Equation (4) allows F_O to be accomplished through F_S . According to the geometrical constraints, δ_S can be considered equivalent to the summation of δ_O and the gap distance between the object and SPA, denoted by G (Figure 9), as follows:

$$\delta_S(t) = \delta_O(t) + G. \quad (5)$$

Equation (5) can be utilized to achieve δ_O through δ_S , when both SPAs have similar behaviours throughout grasping. If the SPAs differently perform on grasping, another correlation should be used for connecting δ_O to δ_S .

3.3 SPA Modeling

The modeling of SPAs has been extensively researched. However, there is still ongoing research on SPA modeling in the field of soft robotics. To handle the infinite DOF structures of SPAs, researchers have commonly employed SPA angle of curvature to represent SPA configuration. Many SPA models based on this representation have been developed under the assumption of constant curvature. Such models are inadequate for SPG pincer grasping. In practice, SPA curvature varies along SPA length. Therefore, a new concept of SPA modeling is required in this case. A possible solution is using δ_S to represent SPA configuration. An SPA model can be initiated based on the equation of motion as follows:

$$\ddot{\delta}_S(t) = f(\delta_S(t), \dot{\delta}_S(t), F_S(t), P_S(t)), \quad (6)$$

where P_S represents the SPA input pressure. The variables $\dot{\delta}_S$ and $\ddot{\delta}_S$ denote the first and second derivatives of δ_S with respect to time, and f represents a nonlinear function that describes SPA nonlinear characteristics. Both $\dot{\delta}_S$ and $\ddot{\delta}_S$ are typically negligible, because SPAs are mostly at their steady state throughout grasping. Equation (6) is then able to be simplified as follows:

$$0 = f(\delta_S(t), F_S(t), P_S(t)). \quad (7)$$

Equation (7) states that δ_S is repeatable under identical conditions of F_S and P_S .

Solving Equation (7) in SPA modeling is well known to be challenging, as there is no standard analytical method available, and accessible simulation solvers are not suitable due to the large deformations and nonlinear characteristics of SPAs. In this study, an empirical investigation was implemented on an industrial SPA (Figure 10). This SPA operates in the P_S range of -100 to 100 kPa, and it weighs 66 gf. The investigation used an experimental setup shown in Figure 11. The experimental setup included a load cell (Figure 12), motorized linear stage (Figure 13), and air supply. The specifications of the load cell and linear stage are respectively expressed in Table 1 and 2.

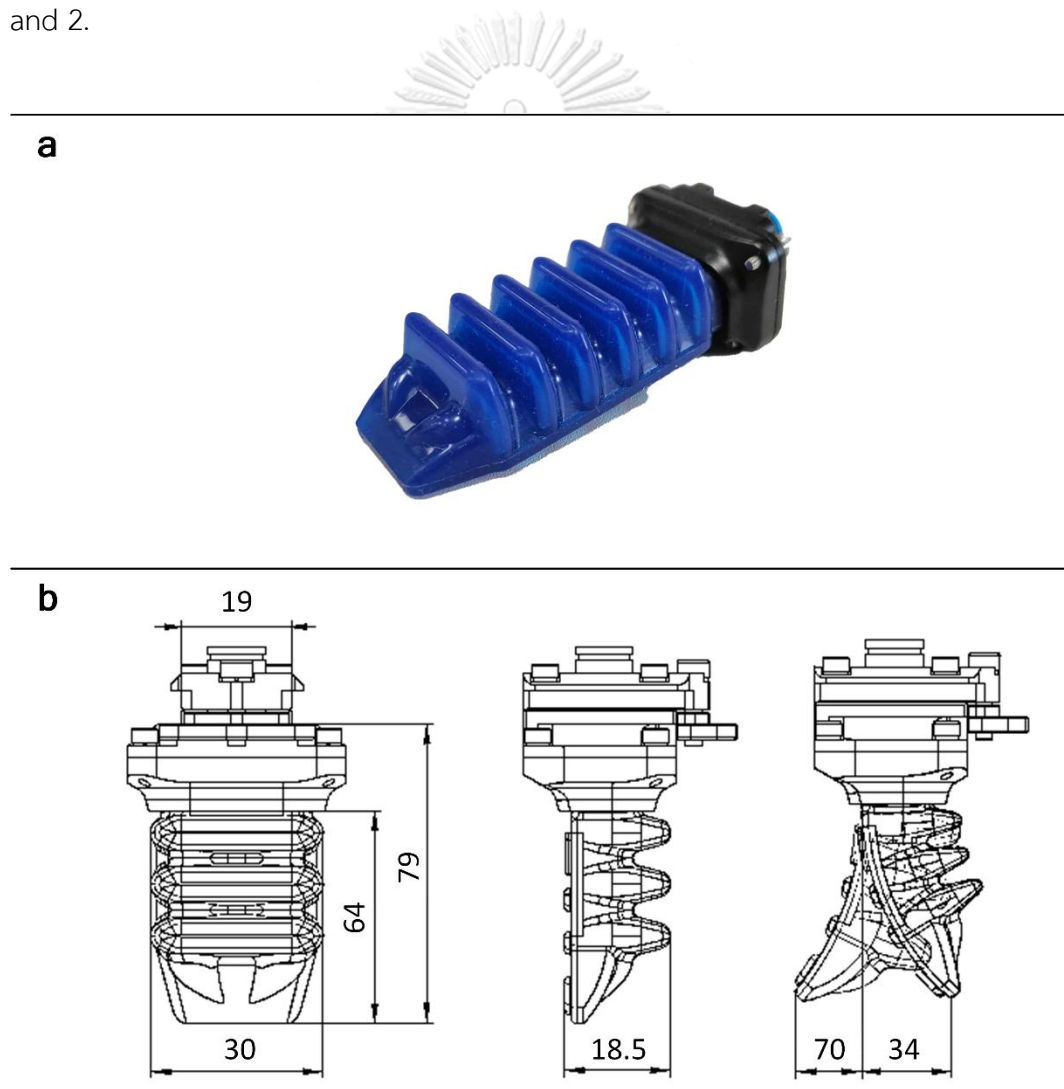


FIGURE 10. SRT M3064 SPA: (a) photograph and (b) dimensional drawing⁸⁹.

The SPA was hung vertically, and the load cell was attached to the linear stage. The load cell was moved horizontally to constrain δ_S , while the air supply generated P_S . The load-cell signal was then interpreted to determine F_S after the SPA reached its steady state under the constrained condition of δ_S and provided value of P_S . This process was repeated for different combinations of δ_S and P_S until F_S was recorded for all designated conditions of δ_S , ranging from 0 to 8 mm with 200- μm intervals, and P_S , ranging from 10 to 100 kPa with 10-kPa increments. Finally, linear fitting using QR factorization⁹⁰ was applied to the resulting relationship between δ_S and F_S at each P_S condition, and the fitting results were plotted as F_S - δ_S straight lines over the δ_S range of 0 to 10 mm.

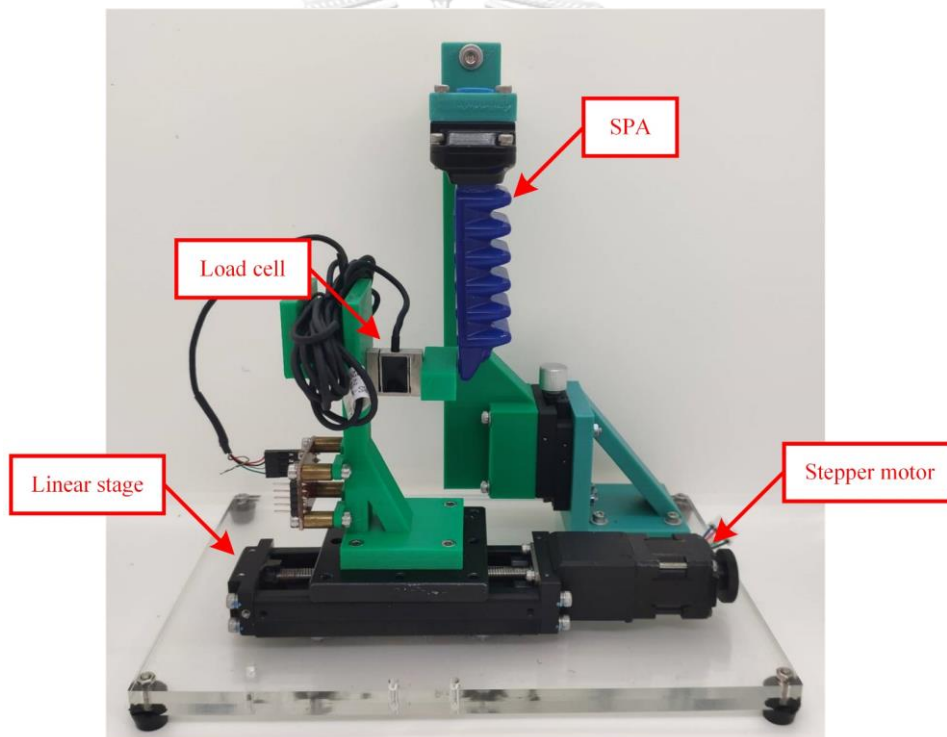


FIGURE 11. An experimental setup for SPA modeling.



FIGURE 12. A miniature s-type load cell.

TABLE 1. Specifications of a miniature s-type load cell.

Attribute	Value
Capacity	1 kgf
Sensitivity	1.5 ± 0.1 mV/V
Creep	0.1 % of FS/hour
Accuracy	0.05 % of FS
Nonlinearity	0.03 % of FS
Repeatability	0.02 % of FS
Allowable load	150 % of FS
Working temperature	-20 to 70 °C
Material	Alloy steel

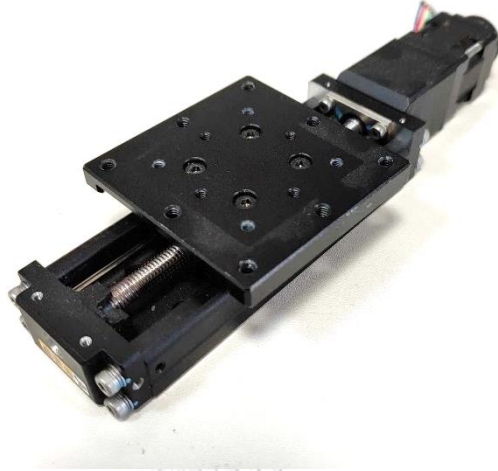


FIGURE 13. A ball-screw linear stage with a 5-phase stepping motor.

TABLE 2. Specifications of a ball-screw linear stage with a 5-phase stepping motor.

Attribute	Value
Motor voltage	0.86 V
Motor current	0.66 A
Motor resolution	0.72°/step
Stage stroke	40 mm
Stage lead	1 mm
Linear resolution	2 $\mu\text{m}/\text{step}$

3.4 Stiffness Sensing Through SPG Pincer Grasping

The proposed method for stiffness sensing relies on object compression due to SPA performance during SPG pincer grasping. Equations (4) and (5) demonstrate that δ_0 and F_0 can be algebraically transformed into δ_S and F_S . Equation (3) can be then revised in accordance with the transformation of δ_0 and F_0 as follows:

$$\partial F_S = k_0(\delta_S - G) \cdot \partial \delta_S. \quad (8)$$

To determine k_0 , a simultaneous series of δ_S and F_S can be produced by varying the applied amount of P_S . The distance G is known from the rest-state geometries of SPGs and grasped objects. However, sensing δ_S and F_S is still challenging. Previous works on

SPA-motion sensing are only based on SPA angle of curvature, which cannot be directly converted into δ_S in SPG pincer grasping. Visual inspection using computer vision is currently the only available approach for immediate observation of δ_S , despite its accuracy. Meanwhile, the sensing of F_S can be achieved only using cutting-edge tactile sensing technologies. Therefore, the most straightforward method for perceiving δ_S or F_S is to utilize computer vision to visually inspect δ_S . Once δ_S is successfully sensed and P_S is identified using some industrial pressure sensors, F_S can be approximated using kinetic models of the SPAs. The method for solving Equation (7), mentioned in the previous section, was developed and implemented for the approximation of F_S .

To demonstrate stiffness sensing through SPG pincer grasping, four elastic elastomer hollow tubes (Figure 14), subsequently call thin, slim, medium, and thick sample, were tested. The hollow tubes were fabricated by 3D printing with the same material, using a fused-deposition-modeling 3D printer with 400- μm extrusion nozzles. Their weight is around 1.5 to 3 g, and their outer diameter was designed to be 20 mm. The major difference between the tubes was their wall thickness. The wall thickness is 800 μm for thin sample, 1.2 mm for slim sample, 1.6 mm for medium sample, and 2 mm for thick sample. The SPG used in this experiment consisted of two SPAs, identical to the one investigated in the previous section. One of the samples was instantaneously grasped in the vertical gesture (Figure 15). Eleven different conditions of P_S , ranging from 0 to 100 kPa with 10-kPa intervals, were applied to the SPG. After each P_S condition, a stereo photograph of the SPG and sample was captured using a binocular digital camera with FHD resolution (Figure 16). The specifications of the binocular camera are shown in Table 3. Afterwards, P_S was released to return the SPG and sample to their neutral shape before repeating the process with another P_S condition. The stereo photographs were then processed using image processing^{91, 92} and stereo computer vision^{93, 94} to estimate the positions, with respect to the camera coordinate system, of the SPA tips. From the estimated positions of the SPA tips, δ_S can be extracted. Meanwhile, G was approximated using a similar process. Once δ_S at each condition of P_S was extracted, the corresponding value F_S was achieved using the SPA model obtained from the experiment addressed in the previous section. Next, the data points at which δ_S was below G or over 10 mm was eliminated, and the x-axis

intersection point was added at $(G,0)$. The remaining pairs of δ_S and F_S were subsequently made continuous using linear interpolation. The characteristics of k_0 were realizable using Equation (8). Alternatively, the resulting δ_S and F_S were converted into δ_0 and F_0 using Equation (4) and (5). The stiffness k_0 was then determined using Equation (3). Two curves of F_0 and k_0 over δ_0 were plotted for demonstration. This process was repeated with all other samples.

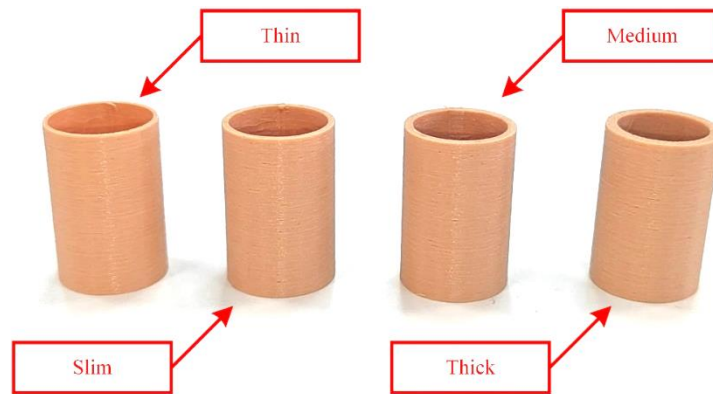


FIGURE 14. Elastic elastomer 3D-printed hollow tubes utilized as testing samples for stiffness sensing.

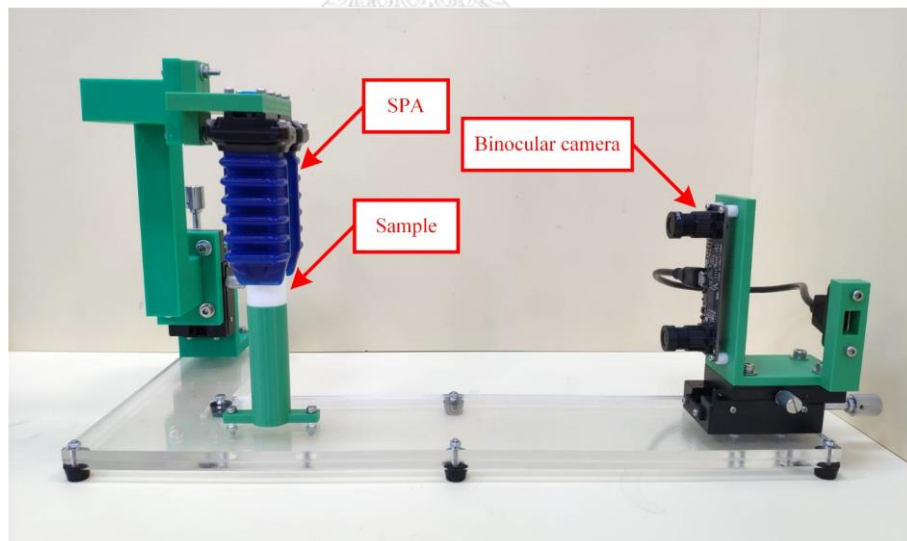


FIGURE 15. An experimental setup for stiffness sensing through SPG pincer grasping.



FIGURE 16. HBV binocular digital camera.⁹⁵

TABLE 3. Specifications of HBV binocular digital camera.

Attribute	Value
Maximum resolution	2560x720 pixels
Maximum refresh rate	30 FPS
Field of view	100°
Pixel size	3 μm
Max dynamic range	72 dB
Sensitivity	2066 mV/(lx·s)
Supply voltage	5 VDC
Power consumption	850 mW

CHULALONGKORN UNIVERSITY

The workflow of image processing and stereo computer vision for approaching δ_S involved several steps. A pair of the stereo photographs was first gone through image undistortion⁹⁶ using pre-calibrated intrinsic camera parameters. Afterwards, the pixels corresponding to the SPA tips were manually extracted from the undistorted images. Point triangulation⁹⁷ was then performed on the extracted pixels to estimate the 3D positions, with respect to the camera, of the SPA tips. The displacement vector from one SPA tip to the other was calculated. The magnitude of the displacement vector was subsequently determined as the distance between the SPA tips. These steps were repeated for every pair of the stereo photographs. The distance between the SPA tips at every P_S condition was determined. The rest-state distance between

the SPA tips was marked as the reference distance. The margins of the distance between the SPA tips at other conditions over the reference distance were considered twice δ_S . This workflow was used for δ_S of every samples.

The determination of G was proceeded with the process similar to the presented workflow of acquiring δ_S . After all pairs of the stereo photographs were undistorted, the edges of the sample were extracted from a pair of the undistorted images. Next, point triangulation was applied to the extracted points of the sample edges. The vector from one of the extracted points to the other was established as the difference of their positions. The magnitude of the vector was considered as the size of the sample. Once the sample size and the distance between the SPA tips were obtained, G can be determined as a haft of the difference of them.

3.5 Validation of Stiffness Sensing Through SPG Pincer Grasping

The validation of the proposed method of stiffness sensing was done by conducting an experiment of compression testing on the same samples. The experimental setup includes a motorized linear stage driven load cell (Figure 17). The load cell and linear stage are identical to the ones used in SPA modeling, the specifications of which are noted in Table 1 and 2. Although this setup was not calibrated, the uncertainty of the setup was calculated from the inaccuracy and resolution of the load cell and linear stage, which resulted ± 44 N/m for k_0 of 1 N/mm. The uncertainty shrinks for greater k_0 , while rises for smaller k_0 . Each sample was compressed using this setup. By moving the load cell, δ_0 was adjusted. The sample was compressed until it was steadily compressed, and then F_0 was measured with the load cell. These steps were iterated until F_0 at all δ_0 conditions, ranging from 0 to 6 mm with 100- μ m intervals, was determined. Afterwards, the corresponding curve of F_0 over δ_0 was plotted. The stiffness k_0 was computed based on the resulting series of δ_0 and F_0 following Equation (3). A curve of k_0 over δ_0 was also plotted for illustration. The resulting k_0 was subsequently compared to its counterpart obtained from the proposed method. The deviation of k_0 , denoted by Δk_0 , was calculated along δ_0 . The definition of Δk_0 was defined as follows:

$$\Delta k_0(\delta_0) = |k_{0,s}(\delta_0) - k_{0,c}(\delta_0)|, \quad (9)$$

where $k_{0,s}$ and $k_{0,c}$ were respectively the values of k_0 gathered from SPG pincer grasping and compression testing. From the resulting Δk_0 , the credibility of the proposed method can be shown.

The viability of the resulting k_0 from the proposed method for object classification was also verified. Manual template-matching classification was implemented on the samples. The classification data was k_0 obtained from the proposed method. Meanwhile, the templates were k_0 collected through compression testing. The classification was proceeded based on the similarity in the moving average of k_0 over δ_0 , and the maximum values in k_0 and δ_0 .

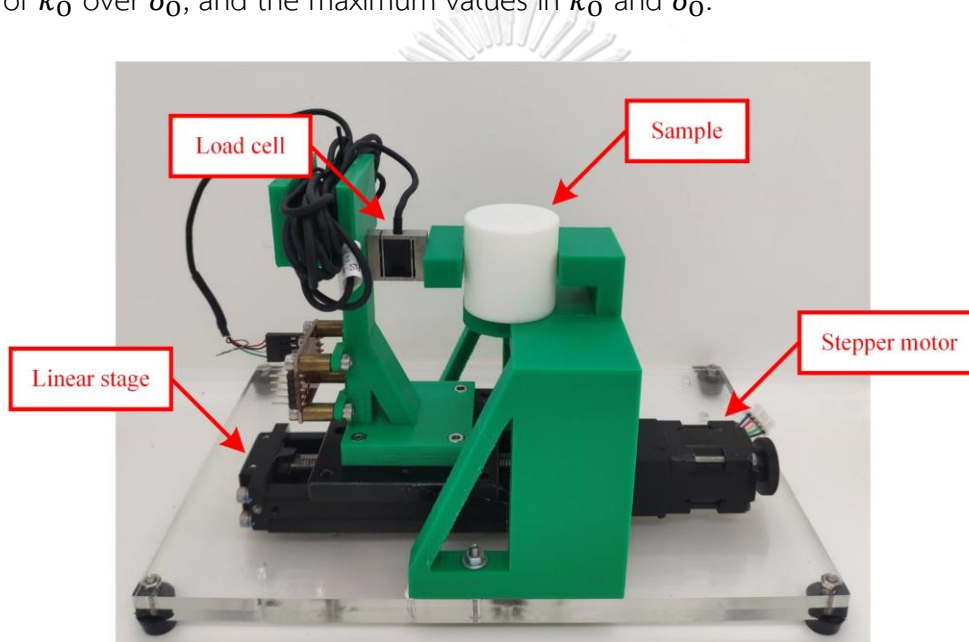


FIGURE 17. An experimental setup for stiffness sensing through compression testing.

3.6 Adaptive SPG Pincer Grasping Based on Object Stiffness

The influence of k_0 on δ_s and F_s throughout SPG pincer grasping can be obviously observed, as demonstrated in Equation (8). By synchronously solving Equation (7) and (8), the resulting δ_s and F_s with respect to P_s during SPG pincer grasping can be foreseen. The presented approach of SPA modeling was developed to solve Equation (7). Furthermore, the proposed method of stiffness sensing basically provides a series of δ_s and F_s in Equation (8) during its process (Figure 18). The corresponding P_s values of the series of δ_s and F_s are also obtained from this framework. Therefore, δ_s and F_s at specific conditions of P_s are predictively

determined. Equation (4) and (5) can be employed to convert δ_S and F_S into δ_O and F_O at the same P_S conditions. By applying linear interpolation on the discrete set of δ_O and F_O , δ_O and F_O can be modeled over a certain range of P_S .

To achieve desirable δ_O and F_O , denoted by δ'_O and F'_O , respectively, a new control architecture is necessary and was consequently elaborated. This control architecture is an opened-loop architecture (Figure 19). First, a suitable amount of P_S for specific δ'_O and F'_O are determined using the technique of modeling δ_O and F_O presented in the previous paragraph. The obtained amount of P_S is subsequently applied to the SPAs of an SPG. If the SPG and object are in an appropriate gesture, SPG pincer grasping is performed. The SPAs operate and produce δ_S and F_S , while the object reacts with δ_O and F_O . Adaptive SPG pincer grasping based on object stiffness is accordingly attainable using this control architecture.

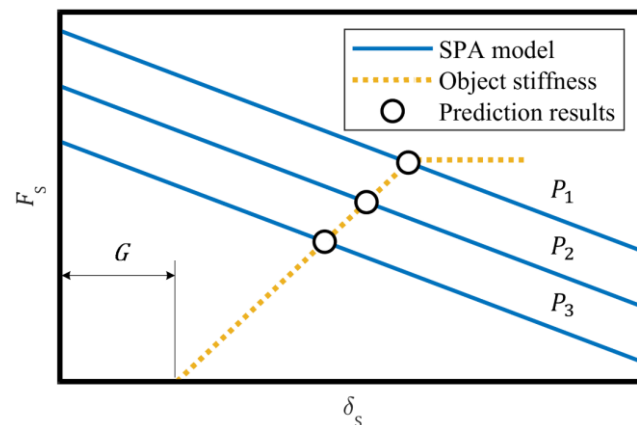


FIGURE 18. A modeling technique for accomplishing adaptive SPG pincer grasping based on object stiffness.

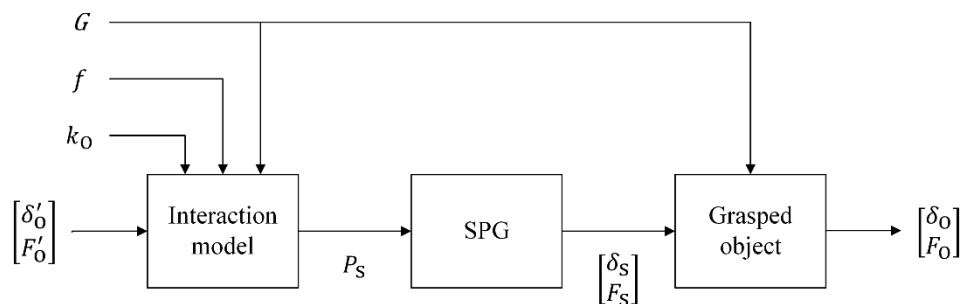


FIGURE 19. An opened-loop control architecture for adaptive SPG pincer grasping based on object stiffness.

The presented technique of modeling δ_0 and F_0 was practiced for demonstration. The resulting δ_S and F_S from the implementation of the proposed method of stiffness sensing were used. The conditions of P_S ranged from 10 to 100 kPa with 10-kPa increments, and there were four testing samples with different k_0 characteristics. Later, δ_0 and F_0 at the same P_S conditions were computed using Equation (4) and (5). Linear interpolation was applied to the resulting δ_0 and F_0 . Hence, δ_0 and F_0 over P_S between 10 to 100 kPa were predicted. Practical SPG pincer grasping was proceeded at the P_S conditions ranging from 25 to 85 kPa with 20-kPa intervals. The corresponding values of δ_0 and F_0 for these P_S conditions were determined using the prediction results, and these values were considered as δ'_0 and F'_0 . Furthermore, δ_0 was practically measured using the same binocular camera previously used for demonstrating the proposed method of stiffness sensing. The workflow of image processing and stereo computer vision for approaching δ_0 was similar to the one employed for determining δ_S and G in that demonstration, but the extracted feature became the locations on the sample edges at which the deformation was largest. From the resulting values δ_0 , F_0 was calculated based on k_0 obtained through compression testing using Equation (3). The difference between δ'_0 and δ_0 , denoted by $\Delta\delta_0$, was subsequently computed together with the difference between F'_0 and F_0 , denoted by ΔF_0 , for evaluating the established technique of adaptive SPG pincer grasping based on object stiffness. Mathematically, $\Delta\delta_0$ and ΔF_0 were defined as follows:

$$\Delta\delta_0(P_S) = |\delta_0(P_S) - \delta'_0(P_S)|, \quad (10)$$

and

$$\Delta F_0(P_S) = |F_0(P_S) - F'_0(P_S)|. \quad (11)$$

CHAPTER IV: RESULTS AND DISCUSSION

4.1 SPA Modeling

An empirical model of the SPA was successfully investigated, and it was the earliest result of this study. The values of F_S at every designated conditions of δ_S and P_S were first obtained (Table 4, APPENDIX A). The linear fitting on each correlation between δ_S and F_S were subsequently succeeded. The resulting coefficients of the linear functions were achieved (Table 5, APPENDIX A). Ten performance curves of the SPA were plotted following the linear functions and utilized as a model of the SPA. The performance curves illustrate the characteristics of F_S over δ_S between 0 and 10 mm, at particular P_S conditions ranging from 10 to 100 kPa with 10-kPa increments (Figure 20). The SPA behaviours during SPG pincer grasping can be then foreseen for this model. At every single condition of P_S , δ_S had a linearly inverse relationship with F_S . The decrease rate of F_S over δ_S varied between 260 and 415 N/m. Moreover, δ_S and F_S were consistently increased over P_S when P_S was amplified. The maximum value of F_S was 2.196 N when δ_S was 0 mm and P_S was 100 kPa, while its minimum value was 0 N when δ_S was 6 mm and P_S was 10 kPa. While the original process was implemented with the of δ_S resolution of 200 μm , it was also proceeded with the δ_S resolutions of 100 and 400 μm . There was tiny changes in the resulting models. The effort and time required for processing SPA modeling of this concept can be reduced with a rougher resolution of δ_S . The increase of SPA curvature along SPA length was also observed in this investigation. The SPA had smaller curvature around its fixed end, and had greater curvature around its free end. This phenomenon consequently highlights the necessity of a new concept of SPA modeling for SPAs operating in SPG pincer grasping.

4.2 Stiffness Sensing Through SPG Pincer Grasping

The implementation of stiffness sensing through SPG pincer grasping was finished. At each condition of P_S , ranging from 0 to 100 kPa with 10-kPa intervals, eleven stereo photographs of SPG pincer grasping were captured and recorded for each testing sample (Figure 26 to 29, APPENDIX B). The mentioned workflow of image

processing and stereo computer vision was further applied on each group of the eleven stereo photographs for determining δ_s and G .

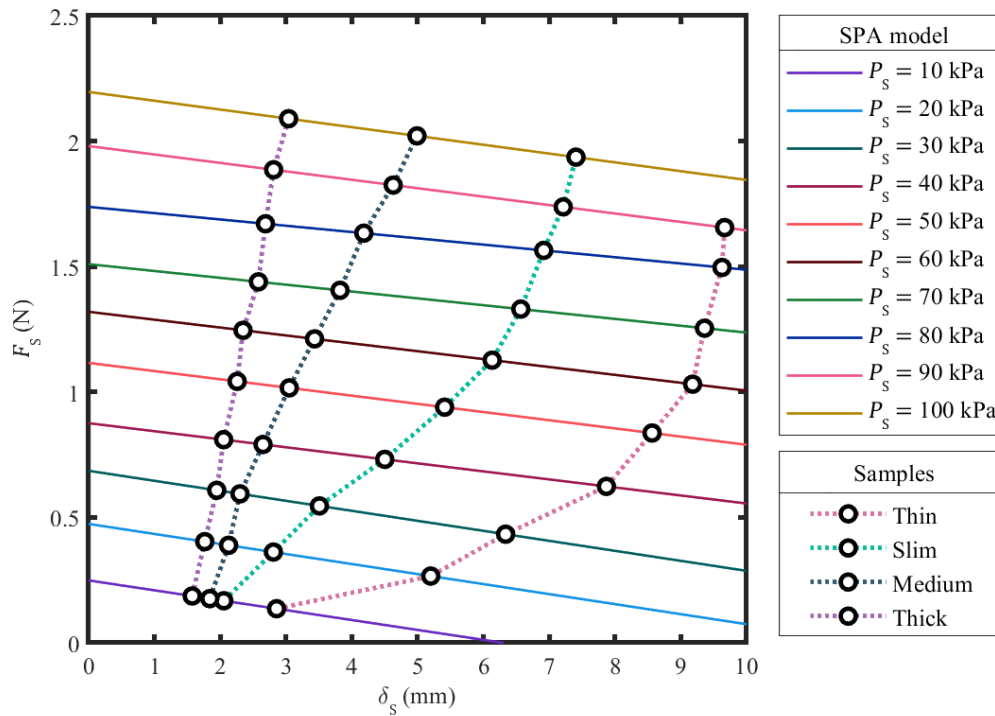


FIGURE 20. An empirical kinetic model of an SPA and primary results of stiffness sensing through SPG pincer grasping on four samples with different stiffness characteristics.

The undistorted images of the stereo photographs were first obtained. The locations of the SPA tips in every pair of the undistorted images were next manually extracted (Figure 21). All extracted pixels are demonstrated in Table 6, 9, 12, and 15, APPENDIX B. This manual procedure took about a haft of hour for each sample, while available solutions of feature extraction⁹⁸ and feature tracking⁹⁹ were unviable in this specific case. This procedure is consequently burdensome nowadays, according to its extremely high consumption in processing effort and time. To overcome this limitation, further studies particularly focusing on feature extraction and feature tracking for deformable objects are strongly recommended. Point triangulation was completed and provided the 3D positions , with respect to the coordinate of the first camera, of the SPA tips (Table 7, 10, 13, and 16, APPENDIX B). From the 3D positions of the SPA

tips, the displacement vector from one SPA tip to the other was calculated, and the distance between the SPA tips was then determined. Afterwards, the values of δ_S at the specific conditions of P_S was achieved. All resulting values of the distance and δ_S are shown in Table 8, 11, 14, 17, APPENDIX B. The corresponding F_S values of the collected series of δ_S were subsequently recognized using the investigated SPA model. The discrete pairs of δ_S and F_S were modified into a continuous correlation between δ_S and F_S . After this process was iterated for all four samples, the correlations between δ_S and F_S in all designated cases were obtained (Figure 20). The resulting δ_S at the P_S condition of 100 kPa for thin sample was not included in the demonstration figure of results, because it was over 10 mm, which was the boundary of consideration in this study.

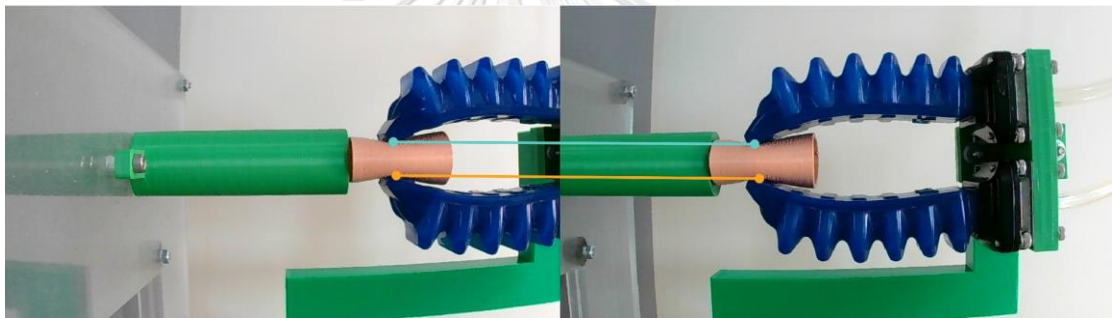


FIGURE 21. A stereo photograph of SPG grasping captured using a binocular camera with manually-extracted features of SPA tips.

From the same set of the undistorted images, the edges of the sample was later manually extracted. The outer diameter of the sample was computed, and found at 20.901 mm for thin sample, 21.129 mm for slim sample, 21.184 mm for medium sample, and 21.244 mm for thick sample. Afterwards, G was calculated and identified at 1.439 mm for thin sample, 1.383 mm for slim sample, 1.27 mm for medium sample, and 1.403 mm for thick sample. Because the samples were all designed to have the same size of outer diameter, and fabricated using the same process and machine, the deviation of the resulting sizes of the outer diameter can be utilized for evaluating the accuracy of the workflow of image processing and stereo computer vision. Thus, the workflow accuracy was concluded as 343 μm .

The equivalent values of δ_0 and F_0 were calculated from G and the resulting series of δ_S and F_S using Equation (4) and (5). Four curves illustrating the values of F_0 over δ_0 were accordingly drawn (Figure 22). The stiffness k_0 of all samples was then computed using Equation (3), and plotted over δ_0 (Figure 22). Consequently, the sensing of k_0 through SPG pincer grasping was successful for all testing samples. The characteristics of k_0 was found as follows:

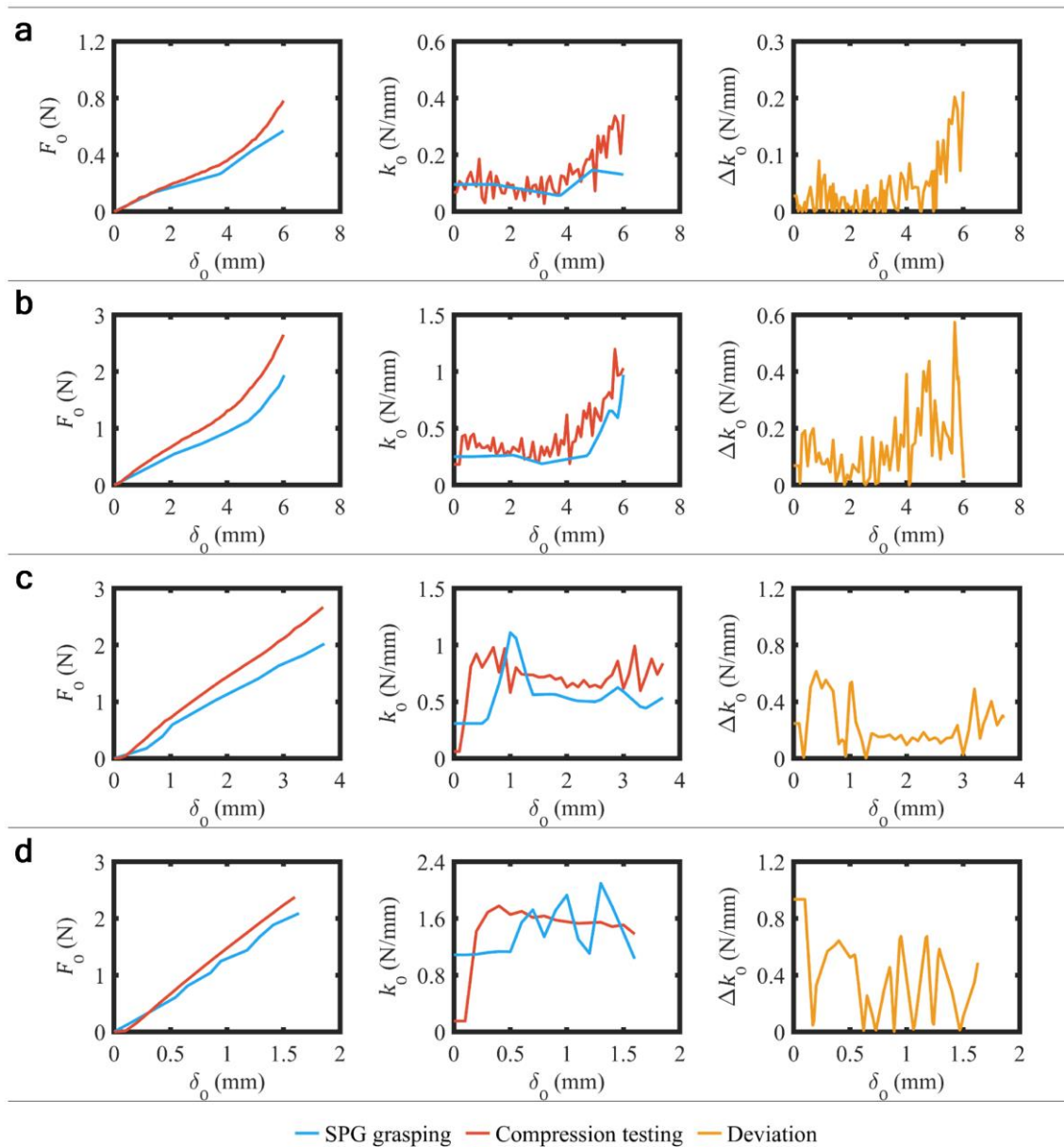


FIGURE 22. Resulting force, stiffness, and stiffness deviations over object deformation from stiffness sensing through SPG pincer grasping and compression testing methods

on four samples with different characteristics of stiffness: (a) thin sample; (b) slim sample; (c) medium sample; (d) thick sample.

- The stiffness k_0 of thin sample slowly dropped from 96 to 57 N/m when δ_0 was below 3.7 mm, then ramped up to 147 N/m when δ_0 was between 3.7 to 4.9 mm, and decayed to 131 N/m when δ_0 was between 4.9 and 6 mm (Figure 22a). For k_0 of this sample at which δ_0 was greater than 6 mm, it dramatically rose over δ_0 , but was not numerically considered, according to the excessive amount of δ_0 .
- The stiffness k_0 of slim sample was horizontal between 188 and 263 N/m when δ_0 was under 4 mm, and dramatically increased to 973 N/m when δ_0 went beyond 4 mm (Figure 22b). The maximum value of δ_0 in the consideration range was 6 mm.
- For medium sample, k_0 over δ_0 was similar to a step response with a single peak of overshoot (Figure 22c). The initial value of k_0 was 308 N/m, and then k_0 ramped up to 1.109 N/mm when δ_0 was between 500 μm and 1 mm. Afterwards, k_0 started to descend from 1.06 N/mm at δ_0 of 1.1 mm to 562 N/m at δ_0 of 1.4 mm. When δ_0 was over 1.1 mm, k_0 was moderately plane between 443 and 625 N/m. The maximum obtained value of δ_0 was 3.7 mm.
- The stiffness k_0 of thick sample was found initially flat between 1.086 and 1.13 N/mm until δ_0 reached 500 μm (Figure 22d). Later, k_0 continuously oscillated between 1.106 and 2.096 N/mm when δ_0 was between 500 μm and 1.6 mm.

4.3 Validation of Stiffness Sensing Through SPG Pincer Grasping

The experiment of compression testing was completed on all four testing samples, and a curve of F_0 over δ_0 was obtained for each testing sample (Figure 22). The raw values of F_0 at all conditions of δ_0 are illustrated in Table 18, APPENDIX B.

Next, k_0 was collected by the calculation on the resulting series of δ_0 and F_0 following Equation (3). The calculated values of k_0 were subsequently drawn over δ_0 (Figure 22). The comparison on the comparable series of k_0 over δ_0 was accomplished. Briefly, k_0 obtained through SPG pincer grasping has similar trends with its counterpart acquired through compression testing. The computation of Δk_0 was successfully finished following Equation (9), and found as follows:

- The deviation Δk_0 of thin sample fluctuated between 0 and 76 N/m when δ_0 was under 4 mm (Figure 22a). Once δ_0 went through 4 mm, Δk_0 increased to 212 N/m at δ_0 of 6 mm. The comparison was terminated at this value of δ_0 .
- For slim sample, Δk_0 frequently oscillated between 0 and 219 N/m when δ_0 was below 4 mm (Figure 22b). Afterwards, the oscillation of Δk_0 became larger, between 0 and 574 N/mm, when δ_0 went beyond 4 mm. The comparison δ_0 conditions ranged from 0 to 6 mm.
- The deviation Δk_0 of medium sample was almost flat between 95 and 233 N/m when δ_0 was between 1.28 and 3 mm (Figure 22c). Out of this range of δ_0 , Δk_0 fluctuated between 0 and 603 N/m. The comparison was done in the δ_0 range of 0 to 3.7 mm.
- For thick sample, Δk_0 was at 934 N/m when δ_0 was smaller than 100 μm (Figure 22d). Later, Δk_0 was roughly oscillating between 0 and 656 N/m when δ_0 ranged from 0 to 1.6 mm.

It was apparently found that Δk_0 was significantly increased when δ_0 grew further than 4 mm, for thin and slim sample (Figure 22a and 22b). The increase of Δk_0 could be caused by occlusion effect¹⁰⁰, which obstructing the visibility of the SPA tips. When δ_0 reaches a certain amount, the SPA tips sink into sample surface, and hence invisible. This phenomenon was occurred when δ_0 was over 4 mm, and made the extracted pixels of the SPA tips deviate from the actual values. Once the extracted pixels were inaccurate, the workflow of image processing and stereo computer vision

provided diverged results of δ_S . Accordingly, the resulting k_0 of the proposed method of stiffness sensing could have large deviations in this region of δ_0 . Future studies on the direct sensing of δ_S are consequently suggested to defeat occlusion effect in the sensing process. If there was an accessible technique for accurate δ_S , the stiffness sensing through the SPG pincer grasping could provide more reliable k_0 over larger ranges of δ_0 .

The manual template-matching classification of all testing samples was also completely done. The resulting values of k_0 over δ_0 obtained through compression testing were plotted for every sample in the same diagram as the templates for classification (Figure 23). The series of k_0 over δ_0 collected through SPG pincer grasping of each sample was individually compared to these templates. The moving average of the k_0 series of thin, slim, and thick sample distinctively matched three different templates, and thus these samples were promptly classified (Figure 23). For medium sample, its series of k_0 have a similar trend with two templates. However, the maximum value in k_0 of the series indicated the matching of this series and the template of medium sample (Figure 23). This classification was not numerically and programmatically done, nevertheless it demonstrates the promise of the proposed method of stiffness sensing to provide credible k_0 for object classification.

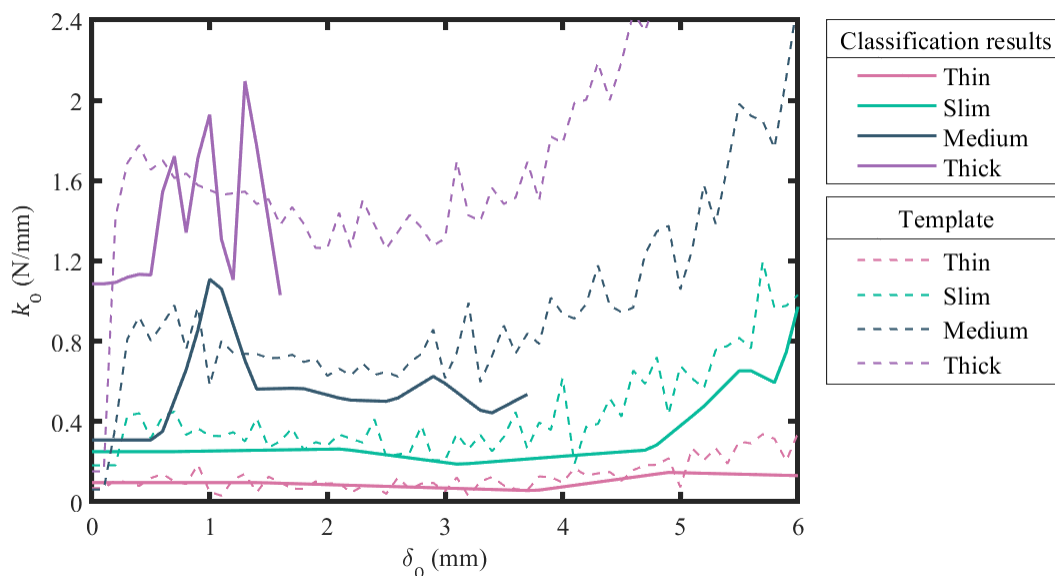


FIGURE 23. Manual classification on four samples based on their stiffness collected through SPG pincer grasping.

4.4 Adaptive SPG Pincer Grasping Based on Object Stiffness

After stiffness sensing through SPG pincer grasping was finished, a pair of δ_S and F_S at every designated condition of P_S , was obtained for each testing sample (Figure 20). The data point at the P_S condition of 100 kPa of thin sample was eliminated, because its δ_S value went beyond 10 mm, which was the consideration boundary. The collected values of δ_S and F_S were converted into δ_O and F_O using Equation (4) and (5), and then plotted over P_S (Figure 24 and 25). Thus, δ_O and F_O were predicted over P_S of 10 to 90 kPa for thin sample, and 10 to 100 kPa for other samples. The values of δ'_O and F'_O were defined equal to the prediction results of δ_O and F_O at the P_S conditions ranging 25 to 85 kPa with 20-kPa intervals. Later, SPG pincer grasping was practiced at the identical conditions of P_S . A stereo photograph of SPG pincer grasping at each P_S condition was successfully collected (Figure 30 to 33, APPENDIX C). The sample edges P_S were manually extracted from the stereo photographs. The extracted pixels of the sample edges are shown in Table 19, 22, 25, and 28, APPENDIX C. The 3D positions of the sample edges were then estimated using point triangulation. The resulting 3D positions are addressed in Table 20, 23, 26, and 29, APPENDIX C. These positions were utilized to calculate δ_O , and the resulting values of δ_O are noted in Table 21, 24, 27, and 30, APPENDIX C. Afterwards, the corresponding values of δ_O were computed based on the results from compression testing. The prediction and actual results of δ_O have resembling tendencies. The comparable values of δ'_O and δ_O were next compared, and $\Delta\delta_O$ were determined (Figure 24). Afterwards, F_O was computed from δ_O and k_O obtained through compression testing using Equation (3). The prediction and actual results of F_O have less similarity compared to the parity of those of δ_O . The comparable values of F'_O and F_O were compared, and ΔF_O was calculated (Figure 25). The maximum values of $\Delta\delta_O$ and ΔF_O for each testing sample can be described as follows:

- The resulting $\Delta\delta_O$ for thin sample was maximum at 375 μm when P_S was at 65 kPa, while ΔF_O was up to 412 mN when P_S was at 45 kPa.

- For slim sample, $\Delta\delta_0$ was highest at 211 μm when P_S was at 45 kPa, and ΔF_0 was greatest at 883 mN when P_S was at 85 kPa.
- The resulting $\Delta\delta_0$ for medium sample was up to 484 μm when P_S was at 85 kPa, and ΔF_0 was largest at 871 mN when P_S was at 85 kPa.
- For thick sample, $\Delta\delta_0$ was up to 456 μm when P_S was at 85 kPa, while ΔF_0 was maximum at 893 mN when P_S was at 65 kPa.

The comparison results show that $\Delta\delta_0$ was under 500 μm . While the accuracy of the sensing of δ_0 was recognized at 343 μm , the resulting values of $\Delta\delta_0$ are acceptable. The resulting ΔF_0 was up to 893 mN, which is relatively high compared to the maximum capacity of the SPAs at 2.196 N. The large values of ΔF_0 could be caused by the superposition effects of Δk_0 and $\Delta\delta_0$. Therefore, further studies on the sensing of δ_S and the association between δ_S and δ_0 , for more accurate results of δ_S and δ_0 are expected to minimize all Δk_0 , $\Delta\delta_0$, and ΔF_0 .

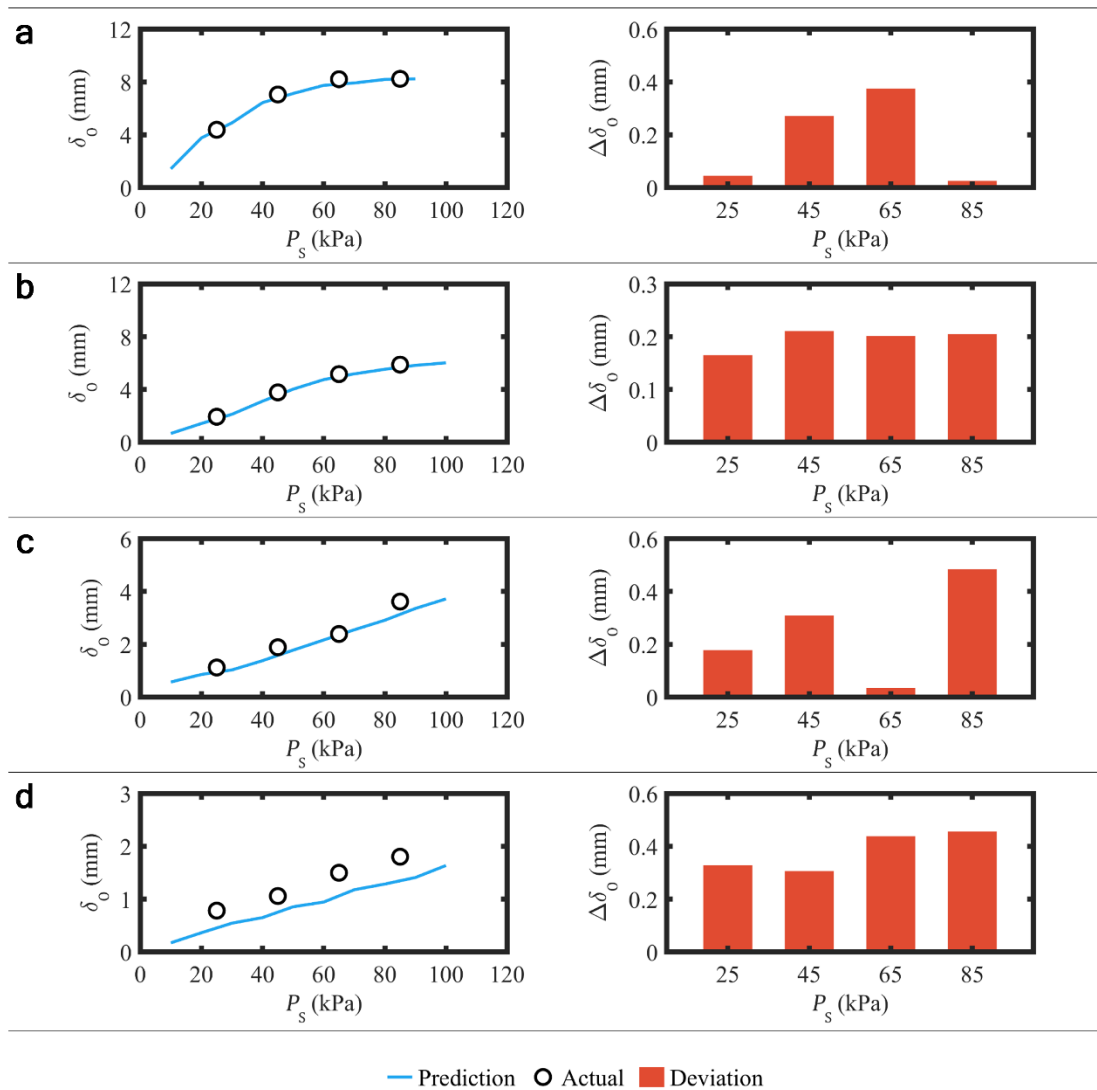


FIGURE 24. Prediction and actual deformation on testing samples in adaptive SPG pincer grasping together with deviations of prediction: (a) thin sample; (b) slim sample; (c) medium sample; (d) thick sample.

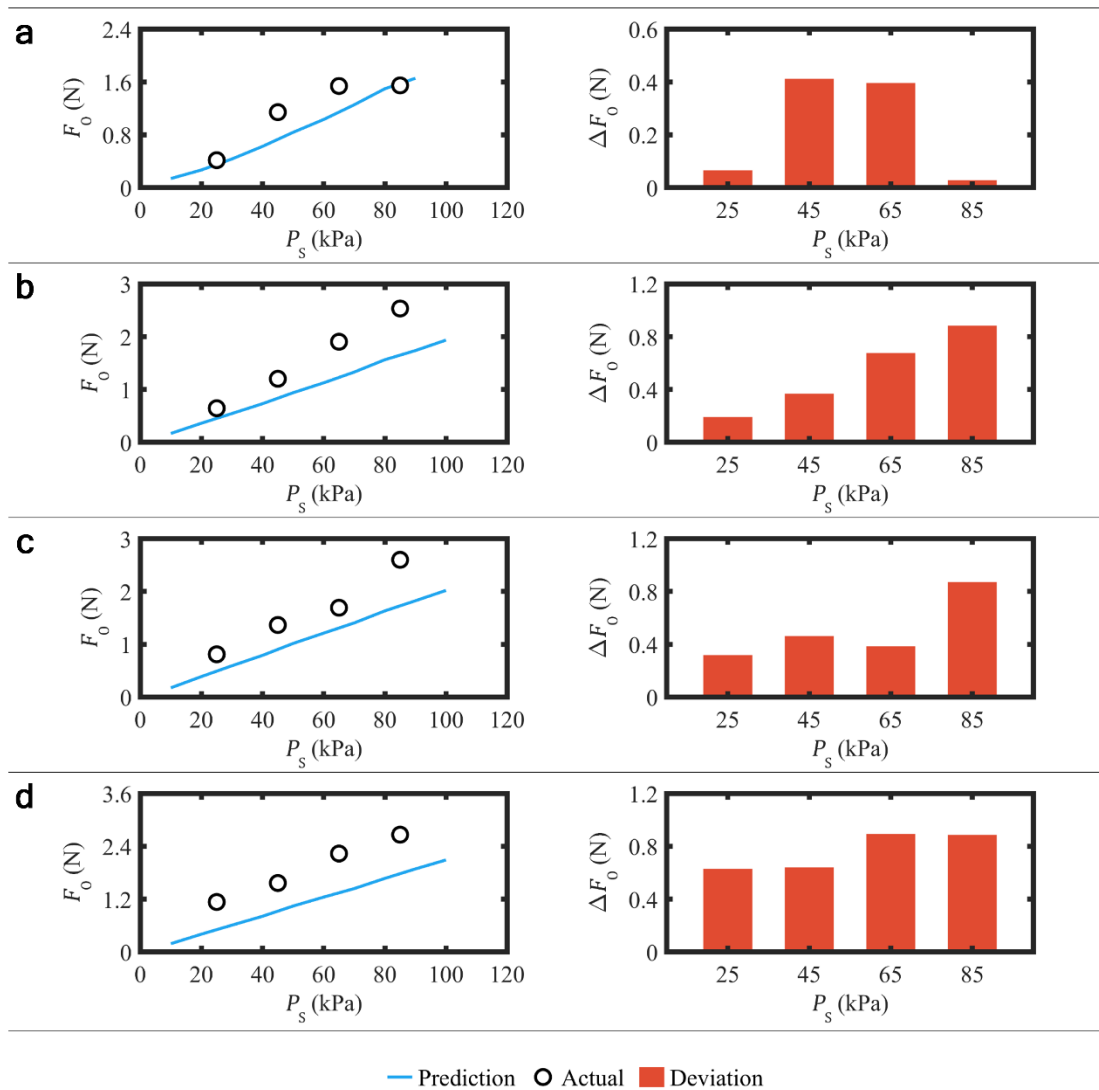


FIGURE 25. Prediction and actual force on testing samples in adaptive SPG pincer grasping together with deviations of prediction: (a) thin sample; (b) slim sample; (c) medium sample; (d) thick sample.

CHAPTER V: CONCLUSION

A framework of stiffness sensing through SPG pincer grasping and adaptive SPG pincer grasping based on object stiffness is comprehensively presented in this study. The purpose of this study is elucidating stiffness sensing through SPG grasping and adaptive SPG grasping based on object stiffness. The transformation between the deformation and force on grasped objects and their equivalents on SPAs is the challenging issue in this study. This challenge is basically caused by the admirable compliance of SPAs, the structures of which have infinite DOF with nonlinear characteristics.

The conventional measurements of object stiffness and its background principle were first revealed, and the connection between stiffness measurement and grasping was addressed. Next, the nature of SPG grasping was analyzed and clarified. The deformation and force on grasped objects during SPG pincer grasping was subsequently associated to their equivalents on SPAs. While available techniques of SPA modeling are constrained to the assumption of constant curvature, SPA curvature is practically increasing along SPA length. Such techniques were thus unviable in this study. A new concept of SPA modeling was later introduced. Afterwards, a method of stiffness sensing through SPG pincer grasping was proposed, and this method was implemented on four cylindrical testing samples with different stiffness characteristics for demonstration. To validate the proposed method of stiffness sensing, compression testing was conducted on the same samples. Furthermore, a technique of forecasting the deformation and force on grasped objects during SPG pincer grasping based on object stiffness was presented. An adaptive opened-loop control architecture of SPG pincer grasping for achieving desirable amounts of the deformation and force on grasped objects was established. To evaluate the forecasting technique and control architecture, SPG pincer grasping was practiced at different conditions of SPA input pressure from the ones at which the SPA operated in SPA modeling. The foreseen and actual values of the deformation and force on grasped objects were finally compared.

The results of stiffness sensing illustrate that the proposed method could provide similar results with their counterparts collected through compression testing, for all testing samples. Moreover, the results of the proposed method of stiffness sensing was viable for manual template-matching classification on the samples. The results of the presented technique of forecasting the deformation and force on grasped objects offered small deviations in deformation, and provided considerable errors in force.

The using of stereo computer vision for the direct sensing of object and SPA deformation was the main limitation in this study, according to its lack of accuracy. Occlusion effect was one of the consequences. This phenomenon obstructed the visibility of the SPA tips, and led to the significant increase of the resulting deviations in all deformation, force, and stiffness. Future studies on the direct sensing of SPA deformation are recommended to overcome this phenomenon, and enhance the resulting accuracy of the proposed framework.

The importance and originality of this study are that it integrates stiffness sensing and SPG grasping into a single action. This study also provides new insights into the utilization of object stiffness in adaptive SPG grasping. The findings of this study should make an important contribution to the field of soft robotics, by associating SPG grasping to a broader range of sensing applications, and leading to a next generation of SPG grasping. Ultimately, this study also contributes to the field of object classification, by providing an efficient framework of acquiring a novel class of classification data.

REFERENCES

1. Siciliano B, Khatib O. *Springer handbook of robotics*. 2nd ed. Springer; 2016.
2. Spong MW, Hutchinson S, Vidyasagar M. *Robot Modeling and Control*. 2nd ed. John Wiley & Sons; 2020.
3. Craig JJ. *Introduction to robotics: mechanics and control*. 4th ed. Pearson; 2017.
4. Pham QC, Madhavan R, Righetti L, Smart W, Chatila R. The Impact of Robotics and Automation on Working Conditions and Employment. Article. *IEEE Robotics and Automation Magazine*. 2018;25(2):126-128.
5. Tsai RY. A New Technique for Fully Autonomous and Efficient 3D Robotics Hand/Eye Calibration. *IEEE Transactions on Robotics and Automation*. 1989;5(3):345-358.
6. Levine S, Pastor P, Krizhevsky A, Ibarz J, Quillen D. Learning hand-eye coordination for robotic grasping with deep learning and large-scale data collection. *International Journal of Robotics Research*. 2018;37(4-5):421-436.
7. Piazza C, Grioli G, Catalano MG, Bicchi A. A Century of Robotic Hands. *Annual Review of Control, Robotics, and Autonomous Systems*. 2019;2:1-32.
8. Marwan QM, Chua SC, Kwek LC. Comprehensive Review on Reaching and Grasping of Objects in Robotics. *Robotica*. 2021;39(10):1849-1882.
9. Han L, Trinkle JC, Li ZX. Grasp analysis as linear matrix inequality problems. *IEEE Transactions on Robotics and Automation*. 2000;16(6):663-674.
10. Miller AT, Allen PK. Graspit: A versatile simulator for robotic grasping. *IEEE Robotics and Automation Magazine*. 2004;11(4):110-122.
11. Bohg J, Morales A, Asfour T, Kragic D. Data-driven grasp synthesis-A survey. *IEEE Transactions on Robotics*. 2014;30(2):289-309.
12. Zhang B, Xie Y, Zhou J, Wang K, Zhang Z. State-of-the-art robotic grippers, grasping and control strategies, as well as their applications in agricultural robots: A review. *Computers and Electronics in Agriculture*. 2020;177
13. Monkman GJ, Hesse S, Steinmann R, Schunk H. *Robot Grippers*. Wiley-VCH; 2006.

14. Yang Y, Chen Y, Li Y, Chen MZQ, Wei Y. Bioinspired robotic fingers based on pneumatic actuator and 3D printing of smart material. *Soft Robotics*. 2017;4(2):147-162.
15. Santina CD, Arapi V, Averta G, Damiani F, Fiore G, Settini A, Catalano MG, Bacciu D, Bicchi A, Bianchi M. Learning from humans how to grasp: A data-driven architecture for autonomous grasping with anthropomorphic soft hands. Article. *IEEE Robotics and Automation Letters*. 2019;4(2):1533-1540.
16. Wang H, Abu-Dakka FJ, Le Nguyen T, Kyrki V, Xu H. A Novel Soft Robotic Hand Design with Human-Inspired Soft Palm: Achieving a Great Diversity of Grasps. Article. *IEEE Robotics and Automation Magazine*. 2021;28(2):37-49.
17. Yoon D, Kim K. Fully Passive Robotic Finger for Human-Inspired Adaptive Grasping in Environmental Constraints. Article. *IEEE/ASME Transactions on Mechatronics*. 2022;
18. Johansson RS, Flanagan JR. Coding and use of tactile signals from the fingertips in object manipulation tasks. *Nature Reviews Neuroscience*. 2009;10(5):345-359.
19. Feix T, Bullock IM, Dollar AM. Analysis of human grasping behavior: Object characteristics and grasp type. Article. *IEEE Transactions on Haptics*. 2014;7(3):311-323.
20. Lederman SJ, Klatzky RL. Haptic classification of common objects: Knowledge-driven exploration. Article. *Cognitive Psychology*. 1990;22(4):421-459.
21. Park J, Moon W. A hybrid-type micro-gripper with an integrated force sensor. *Microsystem Technologies*. 2003;9(8):511-519.
22. Almassri AM, Wan Hasan WZ, Ahmad SA, Ishak AJ, Ghazali AM, Talib DN, Wada C. Pressure sensor: State of the art, design, and application for robotic hand. *Journal of Sensors*. 2015;2015
23. Kappassov Z, Corrales JA, Perdereau V. Tactile sensing in dexterous robot hands - Review. *Robotics and Autonomous Systems*. 2015;74:195-220.
24. Kim DE, Li A, Dau MN, Kim HH, Chung WY. Deep learning-based smith predictor design for a remote grasping control system. *Journal of Mechanical Science and Technology*. 2022;36(5):2533-2545.

25. Calandra R, Owens A, Jayaraman D, Lin J, Yuan W, Malik J, Adelson EH, Levine S. More than a feeling: Learning to grasp and regrasp using vision and touch. *IEEE Robotics and Automation Letters*. 2018;3(4):3300-3307.
26. Girão PS, Ramos PMP, Postolache O, Miguel Dias Pereira J. Tactile sensors for robotic applications. *Measurement: Journal of the International Measurement Confederation*. 2013;46(3):1257-1271.
27. Kim GS. Development of a three-axis gripper force sensor and the intelligent gripper using it. *Sensors and Actuators, A: Physical*. 2007;137(2):213-222.
28. Romano JM, Hsiao K, Niemeyer G, Chitta S, Kuchenbecker KJ. Human-inspired robotic grasp control with tactile sensing. *IEEE Transactions on Robotics*. 2011;27(6):1067-1079.
29. Spiers AJ, Liarakapis MV, Calli B, Dollar AM. Single-Grasp Object Classification and Feature Extraction with Simple Robot Hands and Tactile Sensors. *IEEE Transactions on Haptics*. 2016;9(2):207-220.
30. Spiers AJ, Morgan AS, Srinivasan K, Calli B, Dollar AM. Using a Variable-Friction Robot Hand to Determine Proprioceptive Features for Object Classification during Within-Hand-Manipulation. Article. *IEEE Transactions on Haptics*. 2020;13(3):600-610.
31. Ilievski F, Mazzeo AD, Shepherd RF, Chen X, Whitesides GM. Soft robotics for chemists. *Angewandte Chemie - International Edition*. 2011;50(8):1890-1895.
32. Bao G, Fang H, Chen L, Wan Y, Xu F, Yang Q, Zhang L. Soft robotics: Academic insights and perspectives through bibliometric analysis. *Soft Robotics*. 2018;5(3):229-241.
33. Boyraz P, Runge G, Raatz A. An overview of novel actuators for soft robotics. *Actuators*. 2018;7(3)
34. Bone GM, Lambert A, Edwards M. Automated modeling and robotic grasping of unknown three-dimensional objects. In: *IEEE International Conference on Robotics and Automation*. 2008:292-298.
35. Rus D, Tolley MT. Design, fabrication and control of soft robots. Review. *Nature*. 2015;521(7553):467-475.

36. Thuruthel TG, Ansari Y, Falotico E, Laschi C. Control Strategies for Soft Robotic Manipulators: A Survey. *Soft Robotics*. 2018;5(2):149-163.
37. Hughes J, Culha U, Giardina F, Guenther F, Rosendo A, Iida F. Soft manipulators and grippers: A review. *Frontiers Robotics AI*. 2016;3
38. Hines L, Petersen K, Lum GZ, Sitti M. Soft Actuators for Small-Scale Robotics. *Advanced Materials*. 2017;29(13)
39. Polygerinos P, Correll N, Morin SA, Mosadegh B, Onal CD, Petersen K, Cianchetti M, Tolley MT, Shepherd RF. Soft Robotics: Review of Fluid-Driven Intrinsically Soft Devices; Manufacturing, Sensing, Control, and Applications in Human-Robot Interaction. *Advanced Engineering Materials*. 2017;19(12)
40. Homberg BS, Katzschmann RK, Dogar MR, Rus D. Haptic identification of objects using a modular soft robotic gripper. In: *IEEE International Conference on Intelligent Robots and Systems*. 2015:1698-1705.
41. Chen Y, Guo S, Li C, Yang H, Hao L. Size recognition and adaptive grasping using an integration of actuating and sensing soft pneumatic gripper. *Robotics and Autonomous Systems*. 2018;104:14-24.
42. Sankar S, Balamurugan D, Brown A, Ding K, Xu X, Low JH, Yeow CH, Thakor N. Texture Discrimination with a Soft Biomimetic Finger Using a Flexible Neuromorphic Tactile Sensor Array That Provides Sensory Feedback. *Soft Robotics*. 2021;8(5):577-587.
43. Chu JU, Jung DH, Lee YJ. Design and control of a multifunction myoelectric hand with new adaptive grasping and self-locking mechanisms. 2008:743-748.
44. Zhang W, Che D, Liu H, Ma X, Chen Q, Du D, Sun Z. Super under-actuated multi-fingered mechanical hand with modular self-adaptive gear-rack mechanism. Article. *Industrial Robot*. 2009;36(3):255-262.
45. Wang S, Hu W, Sun L, Wang X, Li Z. Learning Adaptive Grasping From Human Demonstrations. Article. *IEEE/ASME Transactions on Mechatronics*. 2022;27(5):3865-3873.

46. Park S, Hwang D. Softness-Adaptive Pinch-Grasp Strategy Using Fingertip Tactile Information of Robot Hand. Article. *IEEE Robotics and Automation Letters*. 2021;6(4):6370-6377.
47. Chen X, Zhang X, Huang Y, Cao L, Liu J. A review of soft manipulator research, applications, and opportunities. *Journal of Field Robotics*. 2022;39(3):281-311.
48. Su H, Hou X, Zhang X, Qi W, Cai S, Xiong X, Guo J. Pneumatic Soft Robots: Challenges and Benefits. Review. *Actuators*. 2022;11(3)
49. Siciliano B, Sciavicco L, Villani L, Oriolo G. *Robotics: Modelling, Planning and Control*. Springer; 2009.
50. Lipson H. Challenges and Opportunities for Design, Simulation, and Fabrication of Soft Robots. Review. *Soft Robotics*. 2014;1(1):21-27.
51. Hassan T, Cianchetti M, Moatamedi M, Mazzolai B, Laschi C, Dario P. Finite-element modeling and design of a pneumatic braided muscle actuator with multifunctional capabilities. *IEEE/ASME Transactions on Mechatronics*. 2019;24(1):109-119.
52. RG2 Gripper. OnRobot A/S. <https://onrobot.com/en/products/rg2-gripper>
53. Fu H, Zhang W. The development of a soft robot hand with pin-array structure. Article. *Applied Sciences (Switzerland)*. 2019;9(5)
54. Vacuum Grippers. Robotiq Inc. <https://robotiq.com/products/vacuum-grippers>
55. ADHESO Adhesive Grippers. SCHUNK SE & Co. KG. <https://schunk.com/adheso>
56. Mabie H, Reinholtz C. *Mechanisms and Dynamics of Machinery*. 4th ed. Wiley; 1987.
57. Craig JJ. *Introduction to Robotics: Mechanics and Control*. 3rd ed. Pearson; 2004.
58. Bi ZM, Jin Y. Kinematic modeling of Exechon parallel kinematic machine. Article. *Robotics and Computer-Integrated Manufacturing*. 2011;27(1):186-193.
59. Zhang D, Gao Z. Forward kinematics, performance analysis, and multi-objective optimization of a bio-inspired parallel manipulator. Article. *Robotics and Computer-Integrated Manufacturing*. 2012;28(4):484-492.
60. Özgür E, Mezouar Y. Kinematic modeling and control of a robot arm using unit dual quaternions. Article. *Robotics and Autonomous Systems*. 2016;77:66-73.

61. Zi B, Duan BY, Du JL, Bao H. Dynamic modeling and active control of a cable-suspended parallel robot. Article. *Mechatronics*. 2008;18(1):1-12.
62. Chung SJ, Paranjape AA, Dames P, Shen S, Kumar V. A Survey on Aerial Swarm Robotics. Article. *IEEE Transactions on Robotics*. 2018;34(4):837-855.
63. Mousavi S, Gagnol V, Bouzgarrou BC, Ray P. Stability optimization in robotic milling through the control of functional redundancies. Article. *Robotics and Computer-Integrated Manufacturing*. 2018;50:181-192.
64. Denavit J, Hartenberg RS. A kinematic notation for lower-pair mechanisms based on matrices. 1955;
65. Lin PT, Shahabi E, Yang KA, Yao YT, Kuo CH. Parametrically Modeled DH Table for Soft Robot Kinematics: Case Study for A Soft Gripper. 2019:617-625.
66. Goldstein H. *Classical Mechanics*. 2nd ed. Addison Wesley; 1980.
67. Polygerinos P, Wang Z, Overvelde JTB, Galloway KC, Wood RJ, Bertoldi K, Walsh CJ. Modeling of Soft Fiber-Reinforced Bending Actuators. Article. *IEEE Transactions on Robotics*. 2015;31(3):778-789.
68. Huang X, Zou J, Gu G. Kinematic Modeling and Control of Variable Curvature Soft Continuum Robots. Article. *IEEE/ASME Transactions on Mechatronics*. 2021;26(6):3175-3185.
69. Ibrahim S, Krause JC, Olbrich A, Raatz A. Modeling and Reconstruction of State Variables for Low-Level Control of Soft Pneumatic Actuators. Article. *Frontiers in Robotics and AI*. 2021;8
70. Suzumori K, Iikura S, Tanaka H. Applying a Flexible Microactuator to Robotic Mechanisms. Article. *IEEE Control Systems*. 1992;12(1):21-27.
71. Tian Y, Zhang Q, Cai D, Chen C, Zhang J, Duan W. Theoretical modelling of soft robotic gripper with bioinspired fibrillar adhesives. Article. *Mechanics of Advanced Materials and Structures*. 2020;
72. Lotfiani A, Yi X, Shao Z, Zhao H, Parkestani AN. Analytical modeling and optimization of a corrugated soft pneumatic finger considering the performance of pinch and power grasps. Article. *Extreme Mechanics Letters*. 2021;44

73. Haibin Y, Cheng K, Junfeng L, Guilin Y. Modeling of grasping force for a soft robotic gripper with variable stiffness. Article. *Mechanism and Machine Theory*. 2018;128:254-274.
74. Senior AW, Jaimes A. Computer Vision Interfaces for Interactive Art. *Human-Centric Interfaces for Ambient Intelligence*. 2009:33-48.
75. Oliver NM, Rosario B, Pentland AP. A bayesian computer vision system for modeling human interactions. Article. *IEEE Transactions on Pattern Analysis and Machine Intelligence*. 2000;22(8):831-843.
76. Stein GP, Rushinek E, Hayun G, Shashua A. A computer vision system on a chip: A case study from the automotive domain. 2005:
77. Xu Y, Fang G, Lv N, Chen S, Jia Zou J. Computer vision technology for seam tracking in robotic GTAW and GMAW. Article. *Robotics and Computer-Integrated Manufacturing*. 2015;32:25-36.
78. Zhang Z, Trivedi C, Liu X. Automated detection of grade-crossing-trespassing near misses based on computer vision analysis of surveillance video data. Article. *Safety Science*. 2018;110:276-285.
79. Thevenot J, Lopez MB, Hadid A. A Survey on Computer Vision for Assistive Medical Diagnosis from Faces. Article. *IEEE Journal of Biomedical and Health Informatics*. 2018;22(5):1497-1511.
80. Akram T, Naqvi SR, Haider SA, Kamran M. Towards real-time crops surveillance for disease classification: exploiting parallelism in computer vision. Article. *Computers and Electrical Engineering*. 2017;59:15-26.
81. Hartley R, Zisserman A. *Multiple View Geometry in Computer Vision*. 2nd ed. Cambridge University Press; 2004.
82. Yang RS, Lau A, Chan YH, Strozzi AG, Lutteroth C, Delmas P. Bimanual natural user interaction for 3D modelling application using stereo computer vision. 2012:44-51.
83. Murphy-Chutorian E, Trivedi MM. Head pose estimation in computer vision: A survey. Article. *IEEE Transactions on Pattern Analysis and Machine Intelligence*. 2009;31(4):607-626.

84. Micusik B, Pajdla T. Structure from motion with wide circular field of view cameras. Article. *IEEE Transactions on Pattern Analysis and Machine Intelligence*. 2006;28(7):1135-1149.
85. Cabrera EV, Ortiz LE, da Silva BMF, Clua EWG, Gonçalves LMG. A versatile method for depth data error estimation in RGB-D sensors. Article. *Sensors (Switzerland)*. 2018;18(9)
86. Liu Y, Ge Z, Yuan Y, Su X, Guo X, Suo T, Yu Q. Study of the error caused by camera movement for the stereo-vision system. Article. *Applied Sciences (Switzerland)*. 2021;11(20)
87. Smerd R, Winkler S, Salisbury C, Worswick M, Lloyd D, Finn M. High strain rate tensile testing of automotive aluminum alloy sheet. Article. *International Journal of Impact Engineering*. 2005;32(1-4):541-560.
88. Kallio M, Lindroos T, Aalto S, Järvinen E, Kärnä T, Meinander T. Dynamic compression testing of a tunable spring element consisting of a magnetorheological elastomer. Article. *Smart Materials and Structures*. 2007;16(2):506-514.
89. SRT Soft Gripper Selection Manual. Soft Robot Tech Co.,Ltd.; 2020.
90. Subhedar MS, Mankar VH. Image steganography using redundant discrete wavelet transform and QR factorization. Article. *Computers and Electrical Engineering*. 2016;54:406-422.
91. Kruachottikul P, Cooharajanone N, Phanomchoeng G, Chavarnakul T, Kovitangoon K, Trakulwaranont D, Atcharyachanvanich K. Bridge Sub Structure Defect Inspection Assistance by using Deep Learning. 2019:
92. Kruachottikul P, Cooharajanone N, Phanomchoeng G, Chavarnakul T, Kovitangoon K, Trakulwaranont D. Deep learning-based visual defect-inspection system for reinforced concrete bridge substructure: a case of Thailand's department of highways. Article. *Journal of Civil Structural Health Monitoring*. 2021;11(4):949-965.
93. Dadashzadeh M, Abbaspour-Gilandeh Y, Mesri-Gundoshmian T, Sabzi S, Hernández-Hernández JL, Hernández-Hernández M, Ignacio Arribas J. Weed

- classification for site-specific weed management using an automated stereo computer-vision machine-learning system in rice fields. Article. *Plants*. 2020;9(5)
94. Ermilov AA, Baranya S, Török GT. Image-based bed material mapping of a large river. Article. *Water (Switzerland)*. 2020;12(3)
95. HBVCAM OV9732. Huiber Vision Technology Co., Ltd. <https://www.hbvcamera.com/1MP-%20HD-usb-cameras/hbvcam-ov9732-1mp-hd-face-ar-depth-detection-binocular-synchronous-camera-module.html>
96. Zhang M, Hu X, Yao J, Zhao L, Li J, Gong J. Line-based geometric consensus rectification and calibration from single distorted manhattan image. Article. *IEEE Access*. 2019;7:156400-156412.
97. Li J, Bennett BL, Karam LJ, Pettinato JS. Stereo Vision Based Automated Solder Ball Height and Substrate Coplanarity Inspection. Article. *IEEE Transactions on Automation Science and Engineering*. 2016;13(2):757-771.
98. Lowe DG. Distinctive image features from scale-invariant keypoints. Article. *International Journal of Computer Vision*. 2004;60(2):91-110.
99. Senst T, Eiselein V, Sikora T. Robust local optical flow for feature tracking. Article. *IEEE Transactions on Circuits and Systems for Video Technology*. 2012;22(9):1377-1387.
100. Choi IO, Park SH, Kang KB, Lee SH, Kim KT. Efficient parameter estimation for cone-shaped target based on distributed radar networks. Article. *IEEE Sensors Journal*. 2019;19(21):9736-9747.

APPENDIX A: DATA FROM SPA MODELING

TABLE 4. Raw values of SPA force in an experiment of SPA modeling.

δ_S (mm) \ P_S (kPa)	10	20	30	40	50	60	70	80	90	100
0	0.251	0.472	0.692	0.881	1.128	1.336	1.539	1.778	2.012	2.225
0.2	0.241	0.473	0.681	0.874	1.114	1.323	1.534	1.757	2.016	2.223
0.4	0.235	0.466	0.673	0.862	1.111	1.323	1.517	1.756	1.988	2.216
0.6	0.228	0.456	0.662	0.852	1.101	1.313	1.512	1.750	1.990	2.207
0.8	0.214	0.450	0.657	0.848	1.086	1.306	1.502	1.736	1.978	2.190
1	0.210	0.437	0.649	0.838	1.086	1.285	1.493	1.731	1.966	2.179
1.2	0.204	0.434	0.640	0.826	1.078	1.288	1.476	1.720	1.951	2.172
1.4	0.197	0.421	0.627	0.829	1.069	1.278	1.464	1.706	1.942	2.157
1.6	0.186	0.416	0.617	0.818	1.054	1.266	1.457	1.694	1.929	2.146
1.8	0.178	0.405	0.609	0.814	1.054	1.260	1.449	1.686	1.920	2.137
2	0.168	0.388	0.606	0.794	1.047	1.241	1.452	1.675	1.904	2.112
2.2	0.162	0.374	0.596	0.806	1.042	1.238	1.434	1.662	1.897	2.098
2.4	0.154	0.375	0.588	0.806	1.034	1.242	1.433	1.661	1.886	2.086
2.6	0.144	0.361	0.576	0.782	1.029	1.236	1.425	1.655	1.871	2.086
2.8	0.138	0.358	0.569	0.791	1.023	1.232	1.421	1.644	1.864	2.076
3	0.123	0.352	0.559	0.792	1.019	1.229	1.406	1.638	1.855	2.070
3.2	0.118	0.342	0.542	0.786	1.016	1.219	1.405	1.627	1.848	2.074
3.4	0.116	0.335	0.539	0.774	1.005	1.202	1.405	1.634	1.828	2.056
3.6	0.104	0.327	0.544	0.769	0.999	1.202	1.401	1.633	1.833	2.044
3.8	0.100	0.325	0.532	0.767	0.999	1.198	1.391	1.626	1.816	2.039
4	0.090	0.314	0.518	0.750	0.988	1.185	1.388	1.631	1.825	2.027
4.2	0.084	0.304	0.532	0.745	0.981	1.185	1.390	1.619	1.820	2.024
4.4	0.075	0.289	0.522	0.733	0.967	1.194	1.388	1.611	1.815	2.023
4.6	0.065	0.286	0.513	0.729	0.962	1.176	1.380	1.613	1.800	2.022
4.8	0.61	0.276	0.505	0.720	0.954	1.162	1.380	1.614	1.804	2.009
5	0.046	0.270	0.497	0.721	0.943	1.152	1.364	1.608	1.799	1.994
5.2	0.044	0.259	0.487	0.710	0.944	1.136	1.364	1.598	1.794	1.999
5.4	0.037	0.253	0.472	0.709	0.931	1.139	1.363	1.598	1.793	1.993
5.6	0.030	0.240	0.459	0.692	0.928	1.123	1.351	1.592	1.784	1.994
5.8	0.022	0.240	0.457	0.692	0.918	1.116	1.350	1.586	1.783	1.989
6	0.015	0.232	0.452	0.689	0.910	1.123	1.349	1.585	1.773	1.977
6.2	0.006	0.224	0.438	0.688	0.904	1.118	1.335	1.596	1.781	1.969
6.4	0.000	0.226	0.420	0.675	0.909	1.116	1.336	1.561	1.777	1.965

*The values of F_S are in N.

TABLE 4. Raw values of SPA force in an experiment of SPA modeling. (Continued)

δ_S (mm) \ P_S (kPa)	10	20	30	40	50	60	70	80	90	100
6.6	0.000	0.214	0.417	0.661	0.906	1.104	1.343	1.566	1.775	1.959
6.8	0.000	0.205	0.419	0.658	0.891	1.105	1.328	1.557	1.772	1.985
7	0.000	0.200	0.399	0.644	0.894	1.099	1.330	1.573	1.764	1.982
7.2	0.000	0.189	0.387	0.633	0.977	1.106	1.322	1.595	1.759	1.952
7.4	0.000	0.183	0.391	0.637	0.883	1.116	1.298	1.573	1.769	1.939
7.6	0.000	0.179	0.397	0.633	0.875	1.103	1.323	1.574	1.740	1.981
7.8	0.000	0.164	0.365	0.616	0.871	1.084	1.300	1.571	1.731	1.952
8	0.000	0.162	0.369	0.613	0.868	1.091	1.320	1.554	1.728	1.954

*The values of F_S are in N.

TABLE 5. Results of the linear fitting in an experiment of SPA modeling.

P_S (kPa)	$F_S = a\delta_S + b$	
	a	b
10	-0.040	0.249
20	-0.040	0.474
30	-0.040	0.686
40	-0.032	0.876
50	-0.036	1.116
60	-0.031	1.132
70	-0.027	1.510
80	-0.025	1.738
90	-0.034	1.980
100	-0.035	2.196

*The values of δ_S and F_S are respectively in mm and N. The resulting coefficients are with confidence bounces of 95%.

APPENDIX B: DATA FROM STIFFNESS SENSING

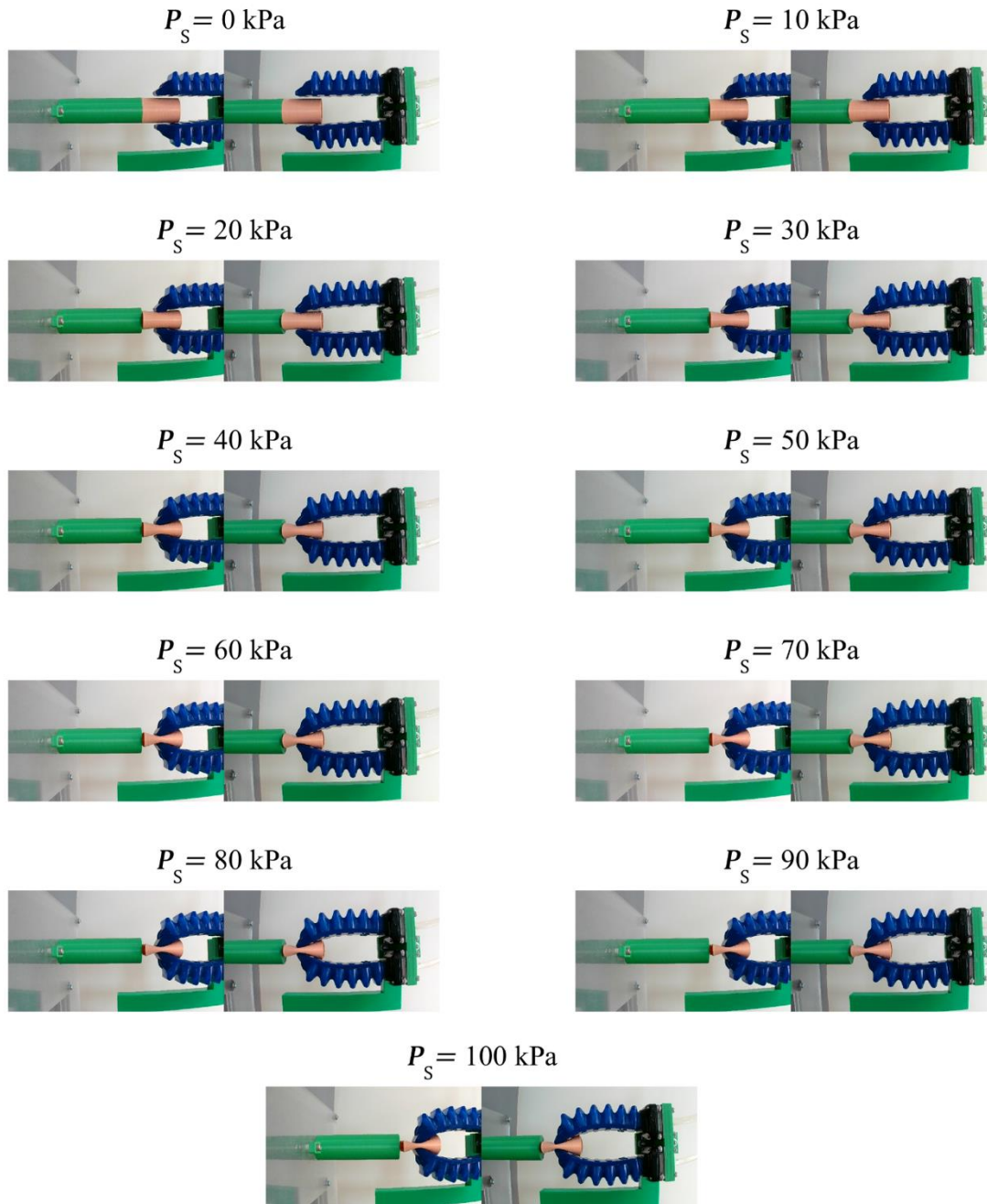


FIGURE 26. Raw stereo photographs of stiffness sensing on thin sample through SPG pincer grasping.

TABLE 6. Extracted pixels of SPA tips from stereo photographs of stiffness sensing on thin sample through SPG pincer grasping.

P_S (kPa)	Left SPA		Right SPA	
	1 st camera	2 nd camera	1 st camera	2 nd camera
0	(894,270)	(446,276)	(893,443)	(453,448)
10	(886,295)	(452,293)	(895,422)	(452,436)
20	(890,309)	(454,323)	(902,394)	(454,407)
30	(895,318)	(451,325)	(912,388)	(454,394)
40	(914,325)	(452,332)	(910,379)	(457,387)
50	(909,329)	(457,335)	(912,374)	(466,381)
60	(907,332)	(454,337)	(915,370)	(464,377)
70	(907,333)	(455,338)	(914,367)	(466,373)
80	(911,335)	(456,341)	(913,365)	(463,371)
90	(914,337)	(452,342)	(917,364)	(461,371)
100	(915,337)	(451,342)	(921,364)	(458,370)

TABLE 7. Estimated 3D positions of SPA tips in stiffness sensing on thin sample through SPG pincer grasping.

P_S (kPa)	Left SPA	Right SPA
0	(33.358,-13.084,186.976)	(33.694,10.440,190.410)
10	(32.979,-10.226,191.696)	(33.311,7.831,192.120)
20	(33.606,-8.161,192.117)	(34.319,4.170,186.975)
30	(33.684,-6.579,188.659)	(34.896,2.821,182.874)
40	(34.867,-5.402,181.276)	(35.012,1.782,184.884)
50	(34.963,-5.053,185.280)	(35.830,1.062,187.752)
60	(34.620,-4.708,184.884)	(35.838,0.514,185.671)

*The positions are in mm with respect to the first camera.

TABLE 7. Estimated 3D positions of SPA tips in stiffness sensing on thin sample through SPG pincer grasping. (Continued)

P_S (kPa)	Left SPA	Right SPA
70	(34.695,-4.584,185.291)	(35.942,0.043,186.908)
80	(34.999,-4.220,184.060)	(35.649,-0.226,186.088)
90	(34.865,-3.959,181.279)	(35.714,-0.289,183.640)
100	(34.846,-3.942,180.499)	(35.700,-0.350,180.866)

*The positions are in mm with respect to the first camera.

TABLE 8. Resulting distance between SPA tips and SPA deformation in stiffness sensing on thin sample through SPG pincer grasping.

P_S (kPa)	Distance (mm)	δ_S (mm)
0	23.778	0.000
10	18.066	2.856
20	13.379	5.199
30	11.104	6.337
40	8.040	7.869
50	6.652	8.563
60	5.419	9.180
70	5.058	9.360
80	4.526	9.626
90	4.446	9.666
100	3.710	10.034

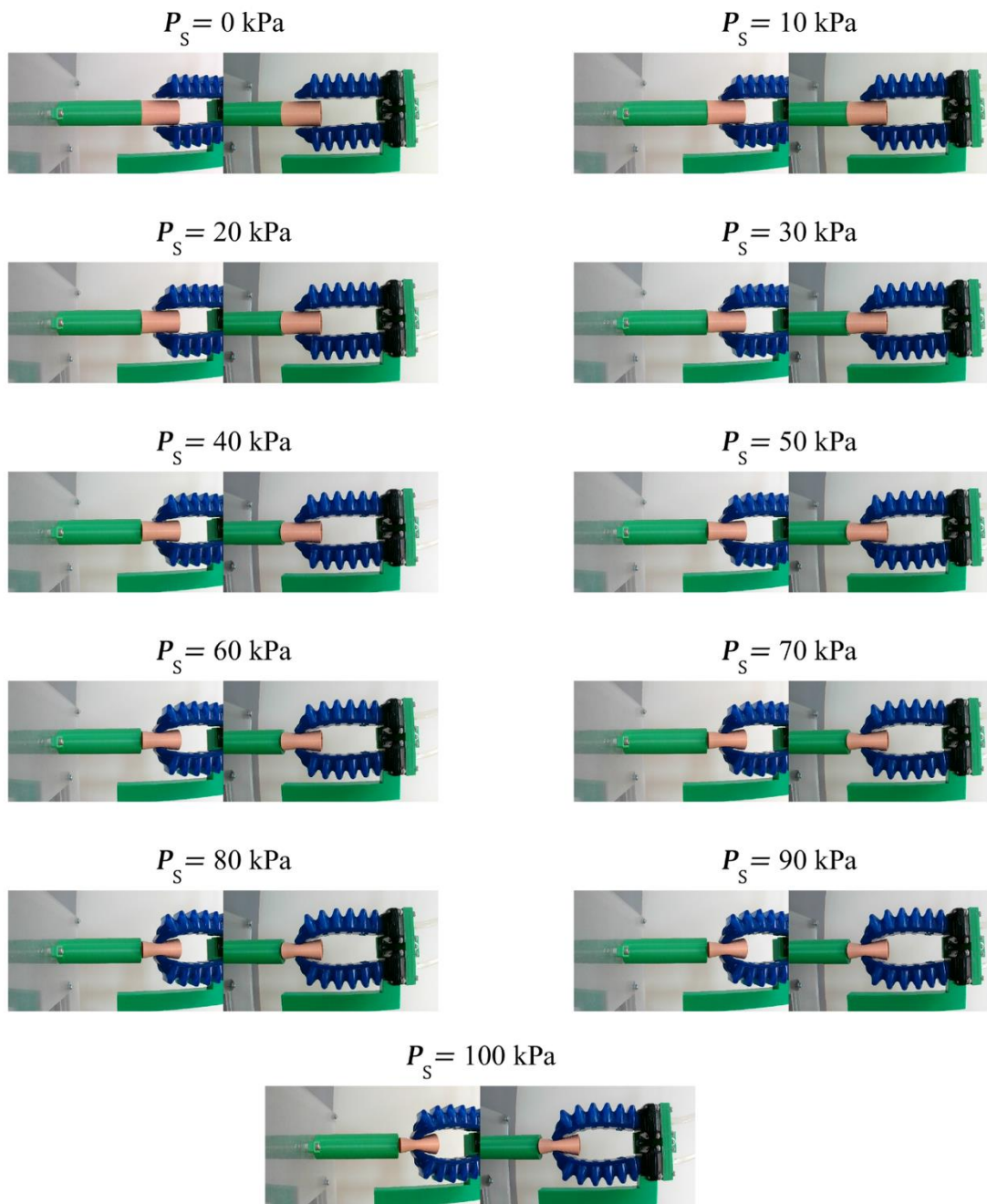


FIGURE 27. Raw stereo photographs of stiffness sensing on slim sample through SPG pincer grasping.

TABLE 9. Extracted pixels of SPA tips from stereo photographs of stiffness sensing on slim sample through SPG pincer grasping.

P_S (kPa)	Left SPA		Right SPA	
	1 st camera	2 nd camera	1 st camera	2 nd camera
0	(888,270)	(447,275)	(891,442)	(453,339)
10	(887,285)	(449,288)	(890,425)	(454,433)
20	(885,291)	(449,293)	(888,419)	(454,427)
30	(885,295)	(448,299)	(887,414)	(454,421)
40	(891,302)	(447,305)	(897,409)	(455,415)
50	(896,306)	(451,312)	(899,402)	(453,408)
60	(895,310)	(452,316)	(896,395)	(453,401)
70	(897,313)	(448,318)	(904,390)	(459,397)
80	(901,315)	(447,321)	(904,385)	(458,392)
90	(899,319)	(448,323)	(904,383)	(461,389)
100	(906,320)	(448,325)	(909,379)	(461,387)

TABLE 10. Estimated 3D positions of SPA tips in stiffness sensing on slim sample through SPG pincer grasping.

P_S (kPa)	Left SPA	Right SPA
0	(32.960,-13.362,189.952)	(33.571,10.489,191.283)
10	(33.044,-11.517,191.253)	(33.588,8.243,192.154)
20	(32.926,-10.805,192.136)	(33.464,7.444,193.041)
30	(32.840,-10.086,191.701)	(33.402,6.690,193.487))
40	(33.142,-9.039,188.673)	(34.095,5.800,189.523)
50	(33.747,-8.267,188.229)	(34.064,4.798,187.824)
60	(33.761,-7.758,189.079)	(33.885,3.872,189.100)

*The positions are in mm with respect to the first camera.

TABLE 10. Estimated 3D positions of SPA tips in stiffness sensing on slim sample through SPG pincer grasping. (Continued)

P_S (kPa)	Left SPA	Right SPA
70	(33.582,-7.317,186.562)	(34.821,3.243,188.215)
80	(33.747,-6.901,184.504)	(34.744,2.556,187.794)
90	(33.702,-6.545,185.732)	(34.978,2.231,189.056)
100	(34.114,-6.245,182.882)	(35.265,1.802,186.936)

*The positions are in mm with respect to the first camera.

TABLE 11. Resulting distance between SPA tips and SPA deformation in stiffness sensing on slim sample through SPG pincer grasping.

P_S (kPa)	Distance (mm)	δ_S (mm)
0	23.896	0.000
10	19.788	2.054
20	18.280	2.808
30	16.881	3.507
40	14.895	4.501
50	13.075	5.410
60	11.630	6.133
70	10.760	6.568
80	10.063	6.916
90	9.470	7.213
100	9.084	7.406

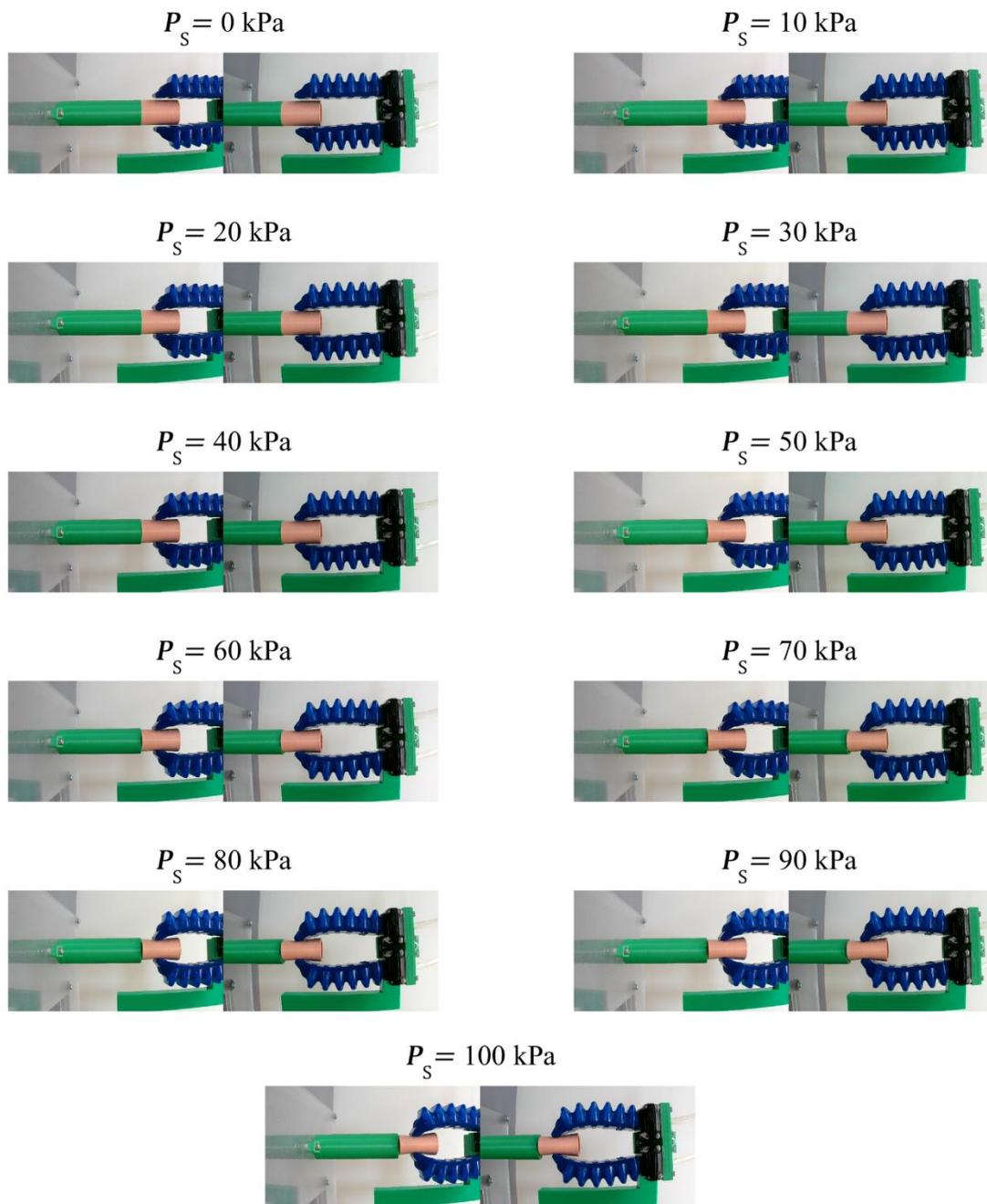


FIGURE 28. Raw stereo photographs of stiffness sensing on medium sample through SPG pincer grasping.

TABLE 12. Extracted pixels of SPA tips from stereo photographs of stiffness sensing on medium sample through SPG pincer grasping.

P_S (kPa)	Left SPA		Right SPA	
	1 st camera	2 nd camera	1 st camera	2 nd camera
0	(890,270)	(447,275)	(894,443)	(450,449)
10	(888,284)	(445,287)	(889,427)	(448,436)
20	(887,288)	(447,289)	(890,425)	(453,433)
30	(896,285)	(447,292)	(895,426)	(453,429)
40	(892,289)	(449,292)	(892,419)	(455,427)
50	(891,291)	(448,296)	(892,417)	(456,422)
60	(890,295)	(448,300)	(887,413)	(454,419)
70	(888,296)	(445,301)	(889,408)	(456,413)
80	(891,298)	(442,303)	(892,404)	(455,409)
90	(892,301)	(443,306)	(894,400)	(457,405)
100	(908,299)	(440,308)	(908,397)	(454,402)

TABLE 13. Estimated 3D positions of SPA tips in stiffness sensing on medium sample through SPG pincer grasping.

P_S (kPa)	Left SPA	Right SPA
0	(33.085,-13.302,189.091)	(33.529,10.415,188.702)
10	(32.810,-11.524,189.105)	(33.072,8.495,189.998)
20	(32.894,-11.190,190.390)	(33.511,8.225,191.717)
30	(33.452,-10.962,186.558)	(33.819,7.924,189.538))
40	(33.355,-10.838,189.087)	(33.789,7.392,191.705)
50	(33.218,-10.427,189.092)	(33.867,6.922,192.140)
60	(33.156,-9.902,189.524)	(33.402,6.480,193.487)

*The positions are in mm with respect to the first camera.

TABLE 13. Estimated 3D positions of SPA tips in stiffness sensing on medium sample through SPG pincer grasping. (Continued)

P_S (kPa)	Left SPA	Right SPA
70	(32.808,-9.744,189.109)	(33.682,5.710,189.109)
80	(32.776,-9.344,186.586)	(33.792,5.103,191.700)
90	(32.911,-8.938,186.582)	(34.081,4.549,191.688)
100	(33.652,-8.572,178.988)	(34.667,3.979,184.494)

*The positions are in mm with respect to the first camera.

TABLE 14. Resulting distance between SPA tips and SPA deformation in stiffness sensing on medium sample through SPG pincer grasping.

P_S (kPa)	Distance (mm)	δ_S (mm)
0	23.724	0.000
10	20.040	1.842
20	19.469	2.128
30	19.123	2.300
40	18.423	2.651
50	17.627	3.049
60	16.857	3.434
70	16.082	3.821
80	15.359	4.183
90	14.467	4.628
100	13.744	4.990

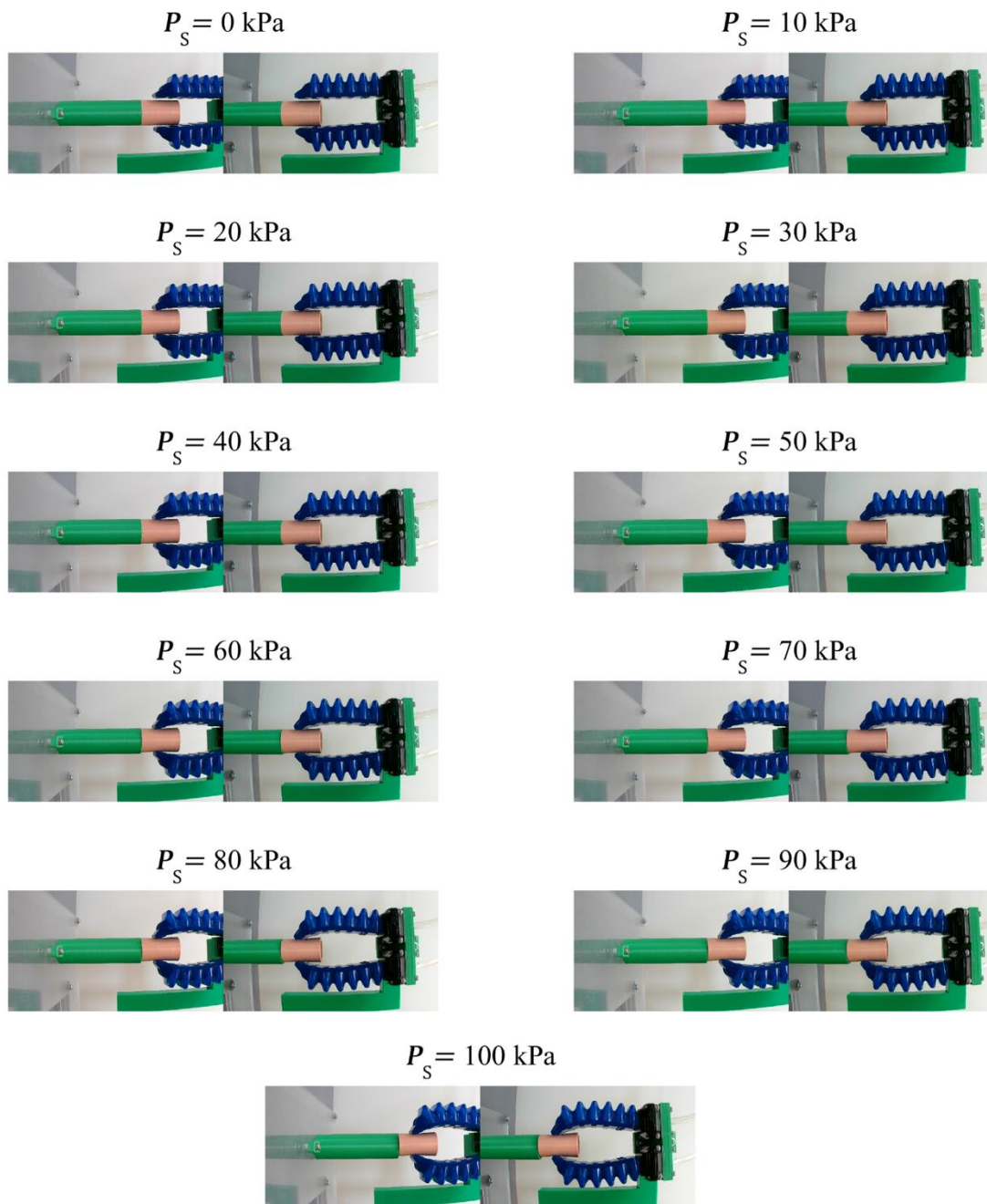


FIGURE 29. Raw stereo photographs of stiffness sensing on thick sample through SPG pincer grasping.

TABLE 15. Extracted pixels of SPA tips from stereo photographs of stiffness sensing on thick sample through SPG pincer grasping.

P_S (kPa)	Left SPA		Right SPA	
	1 st camera	2 nd camera	1 st camera	2 nd camera
0	(891,270)	(447,275)	(893,444)	(455,449)
10	(887,281)	(449,284)	(891,429)	(455,437)
20	(887,283)	(449,287)	(891,428)	(457,436)
30	(887,285)	(449,289)	(887,427)	(454,435)
40	(888,286)	(448,290)	(887,426)	(454,434)
50	(887,287)	(449,291)	(888,425)	(455,432)
60	(891,287)	(445,291)	(889,420)	(456,427)
70	(889,287)	(446,291)	(888,419)	(455,425)
80	(889,288)	(442,292)	(888,416)	(455,421)
90	(894,287)	(443,293)	(891,412)	(456,419)
100	(898,286)	(443,291)	(896,411)	(455,418)

TABLE 16. Estimated 3D positions of SPA tips in stiffness sensing on thick sample through SPG pincer grasping.

P_S (kPa)	Left SPA	Right SPA
0	(33.147,-13.271,188.663)	(33.847,10.626,191.272)
10	(33.044,-12.070,191.252)	(33.726,8.799,192.150)
20	(33.044,-11.724,191.253)	(33.880,8.700,193.028)
30	(33.044,-11.447,191.254)	(33.400,8.580,193.492)
40	(33.032,-11.257,190.386)	(33.400,8.440,193.491)
50	(33.043,-11.170,191.254)	(33.540,8.230,193.485)
60	(32.997,-10.970,187.828)	(33.680,7.530,193.478)

*The positions are in mm with respect to the first camera.

TABLE 16. Estimated 3D positions of SPA tips in stiffness sensing on thick sample through SPG pincer grasping. (Continued)

P_S (kPa)	Left SPA	Right SPA
70	(32.946,-11.044,189.101)	(33.540,7.320,193.483)
80	(32.653,-10.810,187.421)	(33.541,6.830,193.482)
90	(33.036,-10.713,185.747)	(33.805,6.381,192.582)
100	(33.280,-10.818,184.106)	(34.034,6.157,189.956)

*The positions are in mm with respect to the first camera.

TABLE 17. Resulting distance between SPA tips and SPA deformation in stiffness sensing on thick sample through SPG pincer grasping.

P_S (kPa)	Distance (mm)	δ_S (mm)
0	24.050	0.000
10	20.900	1.575
20	20.518	1.766
30	20.155	1.947
40	19.944	2.053
50	19.534	2.258
60	19.355	2.347
70	18.889	2.580
80	18.673	2.688
90	18.426	2.812
100	17.971	3.039

TABLE 18. Raw values of force on samples in compression testing.

δ_0 (mm)	Thin	Slim	Medium	Thick
0.1	0.007	0.018	0.006	0.015
0.2	0.018	0.036	0.044	0.157
0.3	0.027	0.079	0.125	0.326
0.4	0.035	0.124	0.217	0.504
0.5	0.047	0.155	0.298	0.669
0.6	0.061	0.198	0.386	0.839
0.7	0.071	0.243	0.484	1.000
0.8	0.080	0.276	0.560	1.164
0.9	0.098	0.313	0.657	1.322
1	0.103	0.346	0.715	1.477
1.1	0.106	0.378	0.795	1.630
1.2	0.118	0.413	0.869	1.784
1.3	0.132	0.443	0.943	1.938
1.4	0.136	0.485	1.017	2.086
1.5	0.149	0.512	1.088	2.237
1.6	0.158	0.542	1.160	2.375
1.7	0.165	0.579	1.233	2.522
1.8	0.171	0.605	1.303	2.661
1.9	0.182	0.634	1.374	2.787
2	0.191	0.662	1.437	2.914
2.1	0.200	0.696	1.503	3.058
2.2	0.205	0.728	1.566	3.184
2.3	0.212	0.757	1.635	3.334
2.4	0.220	0.798	1.698	3.472
2.5	0.224	0.821	1.763	3.599
2.6	0.237	0.844	1.827	3.733
2.7	0.243	0.869	1.895	3.876
2.8	0.252	0.907	1.969	4.013
2.9	0.261	0.928	2.054	4.140
3	0.267	0.948	2.116	4.272
3.1	0.279	0.982	2.190	4.441
3.2	0.282	1.008	2.290	4.584
3.3	0.292	1.042	2.349	4.724
3.4	0.304	1.067	2.422	4.880
3.5	0.312	1.099	2.510	5.029

*The values of F_0 are in N.

TABLE 18. Raw values of force on samples in compression testing. (Continued)

δ_0 (mm)	Thin	Slim	Medium	Thick
3.6	0.319	1.144	2.584	5.180
3.7	0.325	1.171	2.668	5.350
3.8	0.337	1.210	2.746	5.500
3.9	0.350	1.246	2.848	5.682
4	0.359	1.308	2.942	5.861
4.1	0.376	1.327	3.033	6.059
4.2	0.389	1.364	3.132	6.260
4.3	0.403	1.403	3.249	6.478
4.4	0.418	1.454	3.347	6.679
4.5	0.429	1.497	3.442	6.898
4.6	0.445	1.562	3.538	7.141
4.7	0.463	1.62`	3.662	7.376
4.8	0.481	`693	3.796	7.627
4.9	0.503	1.737	3.934	7.873
5	0.510	1.804	4.040	8.144
5.1	0.537	1.866	4.165	8.409
5.2	0.558	1.922	4.323	8.713
5.3	0.585	2.076	4.461	9.014
5.4	0.604	2.157	4.628	9.340
5.5	0.634	2.234	4.827	9.696
5.6	0.663	2.354	5.019	10.050
5.7	0.697	2.450	5.209	10.384
5.8	0.728	2.548	5.385	10.764
5.9	0.748	2.548	5.596	11.192
6	0.723	2.651	5.848	11.570

*The values of F_0 are in N.

APPENDIX C: DATA FROM ADAPTIVE GRASPING

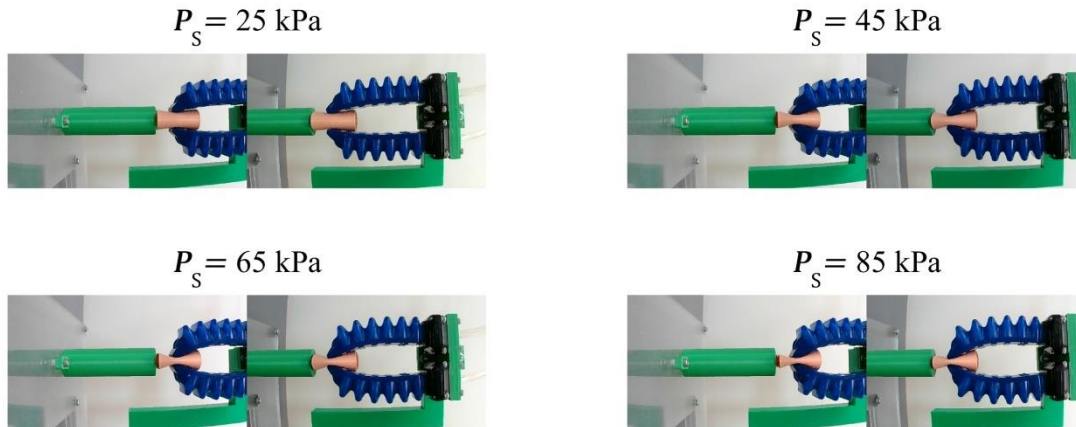


Figure 30. Raw stereo photographs of adaptive SPG pincer grasping on thin sample.

TABLE 19. Extracted pixels of sample edges from stereo photographs of adaptive SPG pincer grasping on thin sample.

P_s (kPa)	Left SPA		Right SPA	
	1 st camera	2 nd camera	1 st camera	2 nd camera
25	(895,315)	(439,322)	(896,414)	(446,401)
45	(903,328)	(444,334)	(907,377)	(442,382)
65	(907,334)	(440,340)	(908,368)	(443,374)
85	(908,336)	(438,342)	(910,366)	(446,370)

TABLE 20. Estimated 3D positions of sample edges in adaptive SPG pincer grasping on thin sample.

P_s (kPa)	Left SPA	Right SPA
25	(32.805, -6.806, 183.729)	(33.362, 5.085, 186.172)
45	(33.644, -5.109, 182.503)	(33.726, 1.279, 180.161)
65	(33.589, -4.243, 179.383)	(33.857, 0.171, 180.154)
85	(33.504, -3.958, 178.242)	(34.191, -0.220, 180.529)

*The positions are in mm with respect to the first camera.

TABLE 21. Resulting distance between sample edges and sample deformation in adaptive SPG pincer grasping on thin sample.

P_s (kPa)	Distance (mm)	δ_0 (mm)
25	12.153	4.374
45	6.804	7.048
65	4.489	8.206
85	4.435	8.233

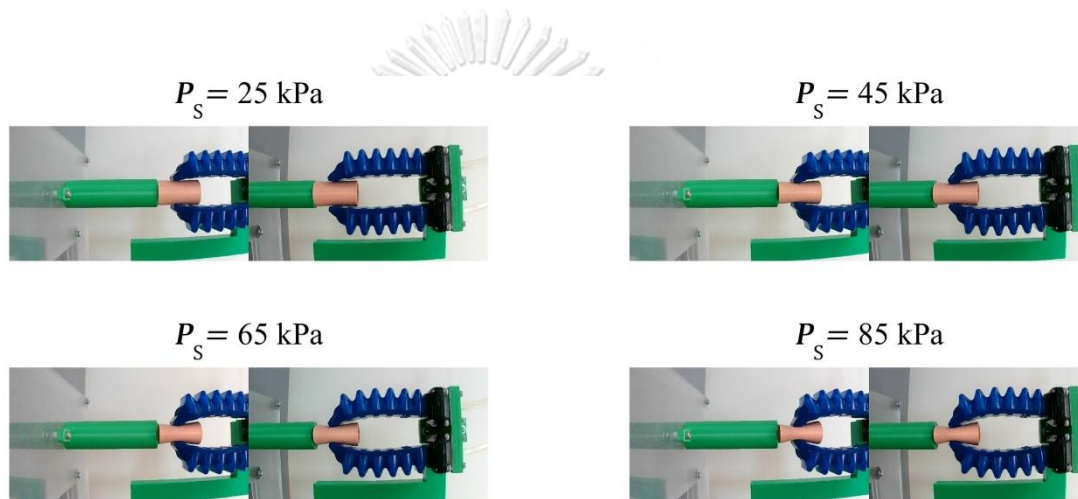


Figure 31. Raw stereo photographs of adaptive SPG pincer grasping on slim sample.

TABLE 22. Extracted pixels of sample edges from stereo photographs of adaptive SPG pincer grasping on slim sample.

P_s (kPa)	Left SPA		Right SPA	
	1 st camera	2 nd camera	1 st camera	2 nd camera
25	(888,293)	(453,299)	(891,416)	(459,422)
45	(892,305)	(445,311)	(899,406)	(448,409)
65	(899,313)	(440,319)	(900,392)	(448,398)
85	(895,317)	(441,323)	(903,384)	(442,390)

TABLE 23. Estimated 3D positions of sample edges in adaptive SPG pincer grasping on slim sample.

P_S (kPa)	Left SPA	Right SPA
25	(33.407,-10.270,192.561)	(34.038,6.916,193.910)
45	(33.056,-8.367,187.412)	(33.689,5.080,185.758)
65	(33.191,-7.107,182.913)	(33.750,3.394,185.342)
85	(32.948,-6.636,184.533)	(33.491,2.276,181.734)

*The positions are in mm with respect to the first camera.

TABLE 24. Resulting distance between sample edges and sample deformation in adaptive SPG pincer grasping on slim sample.

P_S (kPa)	Distance (mm)	δ_0 (mm)
25	17.250	1.940
45	13.563	3.783
65	10.792	5.167
85	9.357	5.886

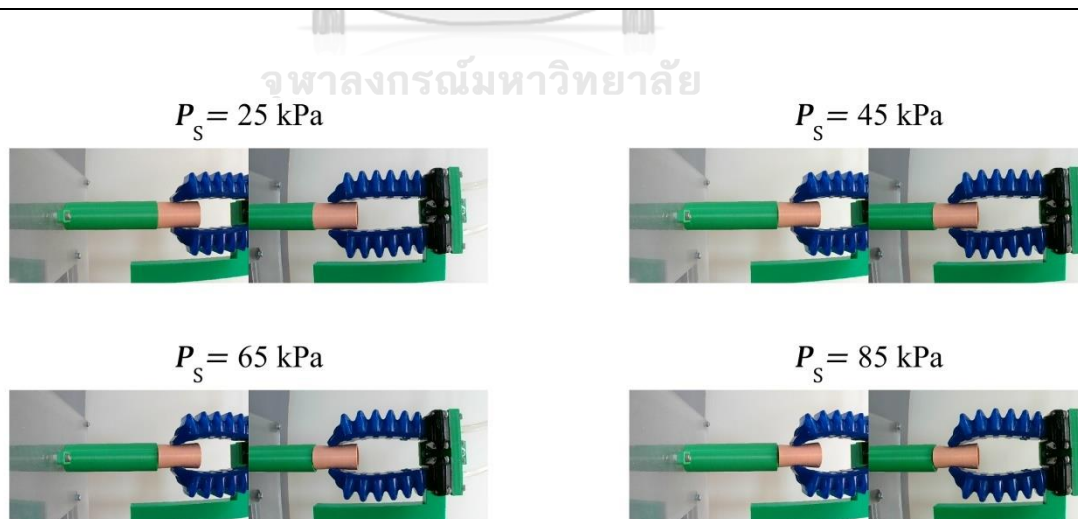


FIGURE 32. Raw stereo photographs of adaptive SPG pincer grasping on medium sample.

TABLE 25. Extracted pixels of sample edges from stereo photographs of adaptive SPG pincer grasping on medium sample.

P_S (kPa)	Left SPA		Right SPA	
	1 st camera	2 nd camera	1 st camera	2 nd camera
25	(889,288)	(453,294)	(889,424)	(456,429)
45	(889,292)	(448,298)	(890,417)	(454,423)
65	(886,297)	(437,303)	(886,411)	(449,417)
85	(891,298)	(441,304)	(893,403)	(443,406)

TABLE 26. Estimated 3D positions of sample edges in adaptive SPG pincer grasping on medium sample.

P_S (kPa)	Left SPA	Right SPA
25	(33.471,-10.942,192.116)	(33.679,7.949,193.479)
45	(33.093,-10.268,189.954)	(33.589,6.992,192.151)
65	(32.103,-9.412,186.610)	(32.960,6.144,191.734)
85	(32.704,-9.255,186.174)	(32.958,4.687,186.197)

*The positions are in mm with respect to the first camera.

TABLE 27. Resulting distance between sample edges and sample deformation in adaptive SPG pincer grasping on medium sample.

P_S (kPa)	Distance (mm)	δ_0 (mm)
25	18.941	1.121
45	17.406	1.888
65	16.401	2.391
85	13.945	3.620

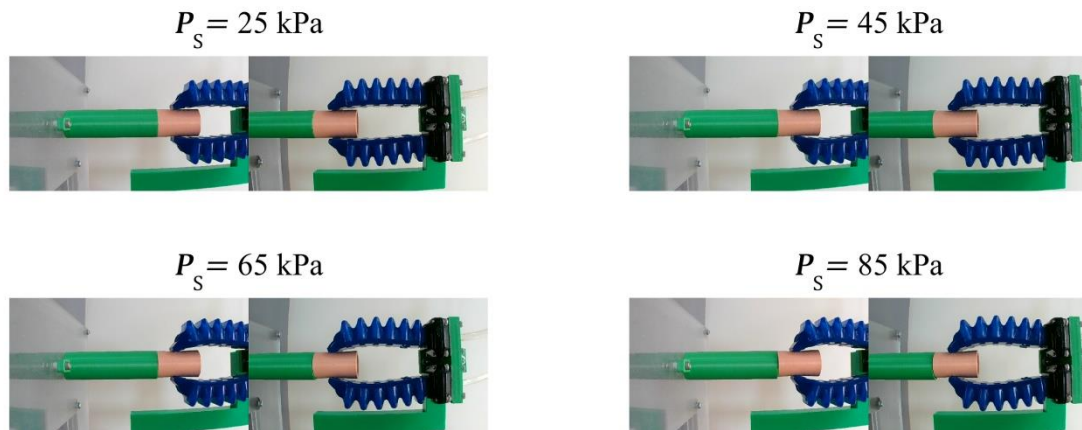


FIGURE 33. Raw stereo photographs of adaptive SPG pincer grasping on thick sample.

TABLE 28. Extracted pixels of sample edges from stereo photographs of adaptive SPG pincer grasping on thick sample.

P_S (kPa)	Left SPA		Right SPA	
	1 st camera	2 nd camera	1 st camera	2 nd camera
25	(888,287)	(452,292)	(892,427)	(456,435)
45	(886,289)	(442,293)	(886,422)	(452,430)
65	(883,285)	(442,292)	(891,418)	(450,424)
85	(883,287)	(441,292)	(890,414)	(441,420)

TABLE 29. Estimated 3D positions of sample edges in adaptive SPG pincer grasping on thick sample.

P_S (kPa)	Left SPA	Right SPA
25	(33.332,-11.151,192.120)	(33.865,8.521,192.120)
45	(32.463,-10.747,188.694)	(33.185,7.862,193.053)
65	(32.272,-11.164,189.982)	(33.348,7.050,189.984)
85	(32.199,-11.002,189.556)	(32.624,6.386,186.628)

*The positions are in mm with respect to the first camera.

TABLE 30. Resulting distance between sample edges and sample deformation in adaptive SPG pincer grasping on thick sample.

P_S (kPa)	Distance (mm)	δ_0 (mm)
25	19.679	0.782
45	19.127	1.058
65	18.246	1.499
85	17.638	1.803



VITA

NAME Chaiwuth Sithiwichankit

DATE OF BIRTH 21 May 1995

PLACE OF BIRTH Bangkok, Thailand

INSTITUTIONS ATTENDED Faculty of Engineering, Chulalongkorn University

PUBLICATION Sithiwichankit C, Chanchareon R. Adaptive Pincer Grasping of Soft Pneumatic Grippers Based on Object Stiffness for Modelling and Controllable Grasping Quality. *Robotics*. 2022; 11(6):132. <https://doi.org/10.3390/robotics11060132>

Sithiwichankit C, Chanchareon R. Advanced Stiffness Sensing through the Pincer Grasping of Soft Pneumatic Grippers. *Sensors*. 2023; 23(13):6094. <https://doi.org/10.3390/s23136094>